REVERSE MICELLE SYNTHESIS AND CHARACTERIZATION OF SUPPORTED BIMETALLIC CATALYSTS

by

Beth A. Cheney

A thesis submitted to the Faculty of the University of Delaware in partial fulfillment of the requirements for the degree of Master of Chemical Engineering

Fall 2010

REVERSE MICELLE SYNTHESIS AND CHARACTERIZATION

OF SUPPORTED BIMETALLIC CATALYSTS

by
Beth A. Cheney

Approved: _____
Jochen A. Lauterbach, Ph.D.
Professor in charge of thesis on behalf of the Advisory Committee

Approved: _____
Jingguang G. Chen, Ph.D.
Professor in charge of thesis on behalf of the Advisory Committee

Approved: _____
Norman J. Wagner, Ph.D.
Chair of the Department of Chemical Engineering

Approved: _____
Michael Chajes, Ph.D.
Dean of the College of Engineering

Approved: _____
Charles G. Riordan, Ph.D.
Vice Provost for Graduate and Professional Education

ACKNOWLEDGMENTS

I would first like to thank my advisors for their contributions to my research and this thesis. Dr. Jochen Lauterbach's comments, criticisms and encouragement during my time at the University helped me to become the researcher and engineer I am today. I also thank Dr. Jingguang Chen for his time and support while completing my thesis and especially during my job search. I greatly appreciate the opportunity he gave me to contribute to collaborations and gain exposure into the world of industrial R&D.

Many thanks also to the faculty and staff of the Chemical Engineering department, particularly Kathie Young for her infinite patience and willingness to answer all of my questions, George Whitmyre and Gary Wellmaker for their enthusiasm to help students, and Dr. Ogunnaike for his time to discuss design of experiments and statistics. I would also like to thank Frank Kriss and Chaoying Ni for their help with microscopy.

I especially appreciate all the hours that members of the Lauterbach and Chen groups put in to support other members during qualifiers, departmental talks, paper and poster edits, performing experiments, and contributing knowledge to set up and troubleshoot equipment. I am especially thankful for Bill Lonergan and Elizabeth D'Addio who served as my mentors during my first year (and beyond). I cannot begin to add up the number of hours they spent to help me both in and outside the lab. I appreciate it and thank them both profusely.

Graduate school would not have been bearable without the friends I have made here, both current students and graduated doctors. Balanced with lab work I enjoyed time spent with friends at house parties, Oktoberfest, girly movie nights, Food and Brew, Woodside Creamery, Wine and Dine, D.C.'s Cherry Blossom Festival, long lunches, and countless coffee breaks. I have also enjoyed the time spent with my fellow IGERTarians during outreach activities, weekly lunches, retreats and conferences. Hydrogen!

I also thank my fiancé Brian who I consider the most successful result of my coming to Delaware. You were always there to make me smile during the hard times and supported me while I made my decisions (and frequently changed my mind about them). I am excited for our future adventures together.

Finally, I want to thank my family. I appreciate the encouragement I have received from my sisters and their families: Jason, Emily and Parker (my "thesis nephew") Hipp and Pete and Sara O'Neill. Last but not least, I acknowledge and thank my parents, Doug and Sharon Cheney, for their unconditional love and endless support not only in graduate school but throughout my entire life. I would not have had all these opportunities without them.

TABLE OF CONTENTS

LIST OF TABLES

LIST OF FIGURES

ABSTRACT

Synthesis of supported nanoparticles with consistent particle size is a bridge between what researchers refer to as the "materials gap," the gap in structure complexity between single crystals and supported catalysts. Controlling particle size during supported catalyst synthesis allows researchers to investigate optimal conditions for desired activity and/or selectivity toward specific chemical reactions. This information can lead to the possibility to tune catalyst synthesis to optimize efficiency and cost while minimizing the waste of precious, nonrenewable resources. This thesis investigates a procedure potentially capable of synthesizing supported catalysts with uniformly-sized nanoparticles. This combines the idealized environment of a model system with the increased complexity associated with nanoparticle size and support effects.

To bridge the materials gap, extensive work has been performed to determine how metallic structures affect adsorbate interactions. Chapter 1 discusses density functional theory (DFT) calculations used to predict adsorbate binding energies on metal monolayer bimetallic surfaces and the correlation to single crystal surfaces and polycrystalline foils. Recently, the trends observed on these model systems have provided insight into enhanced reactivity on oxide-supported bimetallic catalysts.

Due to limitations of particle size control with traditional catalyst synthesis procedures, there is motivation for a method to synthesize uniform particles to better represent model surfaces. Chapter 2 describes reverse micelle synthesis, a technique which has been shown to control nanoparticle size by chemically reducing metal precursors in surfactant-stabilized water droplets suspended in an oil phase.

Techniques used to characterize catalysts synthesized using this method are also discussed in this chapter.

Chapter 3 discusses synthesis of supported monometallic platinum (Pt) and bimetallic platinum-cobalt (Pt-Co) catalysts in aqueous/oil/surfactant microemulsions consisting of water/cyclohexane/Brij-30 reduced by sodium borohydride ($NaBH_4$). Although reverse micelle synthesis produced small (~4 nm) reduced, unsupported nanoparticles, supported particles sintered after high-temperature pre-treatments. Extended X-ray absorption fine structure (EXAFS) measurements confirmed bimetallic bond formations between Pt and Co atoms; however, bimetallic catalysts did not exhibit enhanced hydrogenation activity compared to their monometallic Pt catalysts. A half-fractional factorial design of experiments was implemented to determine what synthesis parameters could be altered to decrease solvent quantities, thus decreasing residual carbon which may have inhibited catalytic activity. Statistical analysis could not be performed due to large scatter between repetitions. Due to unsatisfactory reproducibility involved with this synthesis, an alternative reverse micelle synthesis chemistry was investigated.

The reverse micelle synthesis chemistry described in Chapter 4 incorporated a co-surfactant, which stabilizes surfactant molecules around water droplets and promotes uniformity. The composition was an aqueous/oil/surfactant/co-surfactant microemulsion consisting of water/cyclohexane/Triton X-100/2-propanol. The reducing agent was hydrazine (N_2H_4). Two impregnation methods, step-impregnation and co-impregnation, were tested. Step-impregnation describes the procedure where nickel (Ni) nanoparticles were reduced in microemulsion and supported, followed by depositing Pt using incipient wetness impregnation. Co-

impregnation is the procedure where Ni and Pt were reduced simultaneously in microemulsion and then supported. These methods were compared to catalysts synthesized by incipient wetness impregnation, either step-impregnation (supporting Ni then supporting Pt) or co-impregnation (supporting Pt and Ni simultaneously). Final particle sizes of all catalysts were similar; however, micelle catalysts resulted in a narrower distribution of particle size than those synthesized using only incipient wetness impregnation. Step-impregnated catalysts exhibited enhanced activity compared to monometallic Pt and Ni catalysts, suggesting bimetallic bond formation, which was later confirmed by EXAFS measurements. The co-impregnated micelle catalyst had low activity, comparable to data obtained for monometallic Ni. Bimetallic bond formation could not be measured for the co-impregnated micelle catalyst due to insufficient X-ray absorption during EXAFS measurements. Atomic absorption spectroscopy (AAS) revealed that Pt metal uptake for the co-impregnated micelle catalyst was only 25% of Pt uptake for the incipient wetness catalysts and the step-impregnated micelle catalyst. The low Pt uptake was predicted to be the reason for the low activity and low X-ray absorption.

Chapter 5 discusses challenges associated with reverse micelle synthesis including particle size control, effect of solution pH on metal reduction and adsorption on support, and the effect of pre-treatment conditions on nanoparticle size. To take advantage of the ability to create an idealized environment by controlling particle size to study adsorbate interactions, these challenges must be overcome.

Chapter 1

INTRODUCTION

1.1 Motivation for Fundamental Understanding

Catalyst design is a complicated matter with many options involving metal precursor, support, drying environment, and temperature treatments the catalyst encounters before reaction. Before the 1970s the development of heterogeneous catalysts was considered more as alchemy than science resulting in many trial-and-error experiments. This process was time-consuming, expensive, and did not offer assurances on the final results. Around the 1970s the idea of a scientific basis for the preparation of catalysts was introduced and the incorporation of different sciences began to influence catalyst synthesis.[1] However, even today the design of a new catalyst for a new application is often an improvement of an existing industrial catalyst. What may be a sound procedure to produce a very efficient catalyst for one application may not necessarily be the best choice for another. This leads to a waste of raw materials, which is undesirable given that the majority of metals that exhibit high activity are precious metals that are not only growing scarce but are also very expensive.[2]

In order to limit the trial-and-error approaches associated with catalyst synthesis, researchers use model systems to determine how metals will interact with each other and adsorbates in an attempt to predict reactivity on metallic surfaces. Researchers can support these predictions with surface science experiments to

determine how adsorbates interact with model surfaces, such as single crystals (composed of one crystalline plane) or polycrystalline foils (composed of more than one crystalline plane). However, the industrial catalysts that these surfaces model contain nanoparticles supported on polycrystalline supports whose size may not be uniform, and will contain step and edge sites as well as defects. In order to model reactivity behavior of a supported catalyst, the number of reaction sites must be known and uniform between particles. It is difficult to model activity for non-uniform particles due to variable particle surface area and active sites. Researchers refer to this disconnect between model systems and supported catalysts as the materials gap.

In order to bridge the materials gap between model surfaces studies and supported catalysts, controlled and reproducible synthesis of particles with a narrow particle size distribution is essential. Synthesis of supported nanoparticles would combine the model-like idealized environment of consistent surface area with the complexity of support interactions and available reaction sites that change as a result of particle size. The ability to predict how adsorbates interact with surfaces and to correlate those calculations with oxide-supported catalysts could provide a powerful means to predict how supported catalysts will perform during a desired reaction.

1.2 Correlating Density Functional Theory (DFT) Results with Surface Science Studies

The Chen group has worked extensively to bridge the materials gap by combining density functional theory (DFT) calculations with surface science experiments. Previous researchers have also used these combined studies to better understand bimetallic catalysts due to the enhanced activity and selectivity over their monometallic counterparts.[3] The first step to understanding how a bimetallic

modification affects the activity and selectivity is to understand the interaction between the two metals on an atomic level. DFT calculations are useful to predict the behavior of various catalytic systems based on *ab initio* calculations. The DFT method focuses on solving for electron density rather than solving for individual electrons in order to consider more atoms and construct more realistic metal configurations.[4] This density of states for transition metals is characterized by two bands: the *s*-band and the *d*-band. The *s*-band is broad and often half-filled with one *s* electron in the metallic state. Electrons in the *d* states form narrower bands. The interaction of an adsorbate with the *d* electrons of a metal atom will change the shape of the *d*-bands. When an adsorbate interacts with the broad *s*-band, the adsorbate state broadens and results in a weak chemisorption. When an adsorbate interacts with the narrow *d*-band, split bonding and anti-bonding states result in strong chemisorptions.[5]

One factor that could affect the electronic properties of a metal in a bimetallic surface is the average metal-metal bond length. When surface atom bond lengths are longer than they would be in the bulk they are subjected to tensile strain. The *d*-orbital overlap is decreased which results in a sharpening of the *d*-band and its average energy shifts closer to the Fermi level, resulting in a strong chemisorption. Conversely, when surface atom bond lengths are shorter they are subjected to compressive strain. The *d*-orbital overlap is increased which broadens the *d*-band and its average energy shifts further away from the Fermi level, resulting in a weaker chemisorption. The change in average energy of the *d*-band of the modified metal can be described by its *d*-band center. Given that a shift in *d*-band center corresponds to a change in binding of adsorbates on monometallic systems and that DFT calculations

predict the effect of *d*-band center on adsorption energy, DFT may be used to predict adsorbate interactions with bimetallic surfaces.[4]

There are two main classifications when referring to monolayer bimetallic systems consisting of Pt(111) and 3*d* metals modeled for DFT calculations. The first is a surface configuration, where there is a monolayer of 3*d* metal on top of Pt bulk, denoted as 3*d*-Pt-Pt(111). The second is a subsurface configuration, where the 3*d* metal segregates into the second layer, yielding a Pt-monolayer on the surface, denoted as Pt-3*d*-Pt(111). These configurations have been prepared by physical vapor deposition and studied using DFT and Auger electron spectroscopy by members of the Chen group.[6-8] Depending on the environment, the surface or subsurface configuration is thermodynamically preferred.[4] In the cases of 3*d* = Ni, Co, iron (Fe), manganese (Mn), chromium (Cr), vanadium (V) and titanium (Ti), upon annealing in vacuum or in hydrogen (H_2) the 3*d* metal monolayer surface segregates to the subsurface indicating that the subsurface configuration Pt-3*d*-Pt(111) is more stable. When exposed to oxygen (O_2), the surface structure 3*d*-Pt-Pt(111) is thermodynamically preferred.[9] These same predictions were made for Pt(100) and experiments performed on polycrystalline Pt foils, composed mainly of (111) and (100) planes, followed these same segregation rules.[10]

The importance of the differences between the surface and subsurface structures becomes apparent when comparing adsorbate binding energy, for example that of hydrogen, with *d*-band center on surface and subsurface structures.[11] The farther a metallic configuration is from the Fermi level (that is, a more negative *d*-band center), the lower the hydrogen binding energy (HBE). For subsurface configurations (Pt-3*d*-Pt(111)), HBE is predicted to be weaker. If a metallic configuration has a *d*-

band center closer to the Fermi level, the HBE is higher. For surface configurations (3*d*-Pt-Pt(111)), HBE is predicted to be stronger.[11]

These predictions from DFT calculations correlate well with results from model bimetallic systems prepared experimentally by physical vapor deposition of 1 monolayer (ML) of Ni on Pt(111). DFT calculations predicted that upon annealing in H_2, Ni would segregate into the subsurface layer, resulting in a Pt-surface configuration and lower HBE.[12] When 1 ML Ni/Pt(111) is annealed to 600 K, which is suggested to form a subsurface configuration, a temperature program desorption (TPD) spectrum shows that hydrogen desorbs at 240 K. When no annealing occurs, which has been suggested to yield a surface configuration, hydrogen desorbs at a higher temperature of 353 K.[6] This supports the prediction that annealing in H_2 changes the configuration and correlates well with the prediction that the subsurface configuration results in weaker HBE's.

The same phenomenon was seen on Pt deposited on single crystal Ni(111) for the low-temperature desorption of not only hydrogen but also cyclohexene, benzene, and cyclohexane.[6, 13] In general, hydrogen and alkenes bind more weakly to the subsurface configuration than to the surface configuration and the parent, monometallic surfaces. This configuration has been shown to result in low-temperature hydrogenation pathways in the case of Pt-Ni-Pt(111).[7] The surface configuration, Ni-Pt-Pt(111), binds adsorbates more strongly making it more active for reforming of oxygenates, such as ethylene glycol and glycerol to produce H_2.[14]

Experiments performed on model systems of single crystals and polycrystalline foils appear to correlate well with predictions made from DFT calculations. Of interest is to bridge the materials gap and determine whether the same

observations from model systems correlate to more complex surfaces, such as supported catalysts.

1.3 Correlating Surface Science Experiments with Supported Catalysts

The study of adsorbate binding energies from DFT calculations and surface science experiments predicts that the subsurface configuration resulting from treatment in H_2 should lead to low-temperature hydrogenation pathways. Recent work has been performed to investigate the extent of Pt-Ni bimetallic bond formation on an alumina oxide support (Al_2O_3) and to determine whether weakened adsorbate binding energies result in enhanced hydrogenation activity. In this work, catalysts of varying Pt:Ni molar ratios (1:1, 1:3, and 1:10) and impregnation sequences (Pt-first, Ni-first, co-impregnation) were synthesized.[15]

In the work performed by W.W. Lonergan, activity of the supported Pt-Ni catalyst was analyzed using low-temperature hydrogenation of benzene (343 K) and 1,3-butadiene (308 K). Assuming a first-order reaction rate with respect to benzene or 1,3-butadiene, the rate constants were calculated and are listed in **Table 1.1**. All bimetallic catalysts outperformed their monometallic Pt and Ni parent catalysts and bimetallic activity generally increased with increasing Ni content. Catalysts synthesized with different impregnation sequences did not show a significant difference in hydrogenation activity. All catalysts were pre-treated in H_2 at 723 K, which would result in a subsurface configuration according to previously described DFT and surface science experimental results. The presence of a subsurface Ni configuration which resulted after high temperature pre-treatment in H_2 is an explanation of the enhanced hydrogenation activity.[15]

Table 1.1 First-order consumption rate constants over monometallic and bimetallic catalysts for the hydrogenation of benzene and 1,3-butadiene.[15]

Catalyst	Benzene k (min^{-1})	1,3-Butadiene k (min^{-1})
3Ni/γ-Al_2O_3	~0	1.3×10^{-3}
1Pt/γ-Al_2O_3	2.5×10^{-3}	1.4×10^{-2}
1Pt-1Ni/γ-Al_2O_3	4.4×10^{-3}	4.0×10^{-2}
1Pt-3Ni/γ-Al_2O_3	4.1×10^{-3}	4.8×10^{-2}
1Pt-10Ni/γ-Al_2O_3	6.5×10^{-3}	1.6×10^{-1}

The previous discussion shows that surface science experiments correlate well with experiments performed on supported bimetallic catalysts. DFT calculations can be used to investigate adsorbate bonding on surface and subsurface configurations to provide insightful predictions for reactant activity on both model surfaces and oxide-supported catalysts. Using the calculations as a predictive measure would decrease expensive and time-consuming experiments and could lead to more efficient catalyst synthesis and experimental designs.

1.4 Influence of Oxide Support and Metal Particle Size on Reactivity

Supported catalysts often exhibit unique activity depending on the shape and size of metal nanoparticles. Such reactions that are affected by the structure of metal nanoparticles are called structure- or surface-sensitive reactions. Progress in computational catalysis and surface science experiments has lead to an enhanced theoretical understanding of how particle size and shape affects reactivity in catalytic systems. A recent account by van Santen describes different classes of reactions and their dependence on diameter.[16]

One example of a surface-sensitive reaction is a reaction involving the cleavage of formation of molecular π-bonds, as in CO or nitrogen (N_2). The activation of these bonds requires a reaction center with a unique configuration of several metal atoms and step-edge sites, which cannot be physically present on particles smaller than 2 nm. Therefore, the rate of reaction will sharply decrease when particle size is below a critical size. An example of the limitation of particle size in this type of reaction is ammonia decomposition on ruthenium (Ru) nanoparticles.[16] Researchers in the 1960s noted B5 sites, unique step-edge type sites, on particles with the shape of incomplete octahedral.[17] These sites cannot physically exist on particles smaller than 2 nm. Years later, surface science studies and computational studies confirmed the uniqueness of B5 sites for dissociation of nitrous oxide (NO)[18] and N_2[19] at the surface step edges of Ru(0001).

The activation of σ chemical bonds, in which the activation proceeds at a single metal atom, is an example of another surface-sensitive reaction. The rate of a surface atom sensitive reaction, such as the dissociative adsorption with cleavage of a CH bond, will increase with decreasing particle size, since the surface area (thus number of surface atoms) and the number of low-coordinated sites increase.[16] Researchers have observed an increase in normalized conversion rates for catalytic reactions involving CH bond activation of methane on Pt[20] and Ru-based[21] catalysts with decreasing particle size.

The reverse reaction of the cleavage of a CH bond, hydrogenation, is typically independent of particle size and thus structure-insensitive. The rate-limiting step for these reactions is the recombination of an adsorbed hydrogen atom with the

surface alkyl intermediate and the formation of a σ-type bond.[16] Therefore catalytic activity is not a function of the rate of adsorption of molecules.

Not only are model systems limited by the lack of representation of effect on shape and structure in supported catalysts, but the effect of the support itself. In one experiment, gold (Au) nanoparticles supported on TiO_2, $MgAl_2O_4$ and Al_2O_3 significantly affected the diameter and geometry of the nanoparticles. Geometric models based on types of atoms (edge, corner, surface atoms not in contact and in contact with support) were constructed based on 1500-2000 particles found using scanning transmission electron microscopy. Au/TiO_2 was about twice as active for CO oxidation compared to $Au/MgAl_2O_4$ and Au/Al_2O_3. The difference in activity between Au/TiO_2 and $Au/MgAl_2O_4$ matched the difference of low-coordinated Au atoms located at the corners of the Au nanoparticles not in contact with the support. This difference in Au particle geometry is an explanation for why different catalytic activity is observed on a reducible (TiO_2) and irreducible ($MgAl_2O_4$) support. The turnover frequency (TOF) for Au/Al_2O_3 is 4-5 times lower than that for Au/TiO_2 and $Au/MgAl_2O_4$, illustrating that the support can still impact the catalytic activity of the particles that is not directly related to the number of low-coordinated gold atoms.[22]

Structure-sensitive reactions and support effects are just two of many challenges for researchers interested in designing efficient catalysts. While DFT calculations and model systems provide powerful means to predict and investigate adsorbate interactions on surfaces which can elucidate meaning behind chemical reactivity, there is a limitation to the extent of complexity these systems can represent. An understanding of how reactions proceed on supported catalysts is crucial for designing industrial catalysts for various applications.

1.5 Limitations in Industrial Catalyst Synthesis

Wetness impregnation and incipient wetness impregnation are widely used in industry to synthesize monometallic and bimetallic nanoparticles. Wet impregnation involves dissolving the metal salt in excess water and then contacting this solution with support. After a certain time the solid is separated and the excess solution is removed by drying. This differs from incipient wetness impregnation, which involves dissolving the metal salt in a volume of water equal to or slightly less than the pore volume of the support, then mixing with support. This point of saturation is referred to as reaching the point of "incipient wetness." In this case the maximum loading of the support is limited by the solubility of the precursor in the solution. The main control of particle size in both techniques is the temperature, which influences the precursor solubility and solution viscosity. The concentration profile of the impregnated solution depends on mass transfer conditions within the pores during impregnation and drying, which is affected by the surface area and pore volume of the support.[23]

After impregnation, catalysts often undergo drying, calcination and/or heating treatments. Drying refers to the elimination of the solvent (often water) from the pores of the solid. Calcination refers to heating without the formation of a liquid phase and is a further heat-treatment beyond drying. When an atmosphere besides air is employed (N_2, O_2, vacuum, etc.) the term heating is often used rather than calcination. Many processes occur during calcination and heating: loss of physically and chemically bonded water (H_2O) or carbon dioxide (CO_2), modification of the nature and/or structure of the phases present, and sintering, which is the formation of larger particles from small particles. The goal is to optimize a calcination/heating ramp, temperature and environment that minimize sintering as much as possible, since

larger particles reduce the amount of surface area available for reaction and can affect the sites on which reactions take place.[1] Published literature contains many accounts of the difficulty of maintaining narrow particle size distributions using wetness and incipient wetness impregnation.[15, 24]

Given the variability in nanoparticle size and shape while synthesizing using impregnation methods, it is difficult to understand reaction pathways when reactions are performed on industrial catalysts. In order to understand how activity and selectivity are affected by active sites on nanoparticles, the ability to synthesize supported nanoparticles with consistent particle size is crucial. Gaining control during supported catalyst synthesis allows researchers to investigate the optimal nanoparticle size and shape for certain reaction pathways. This can lead to optimizing activity and/or selectivity of chemical reactions. This information can be communicated to industry leaders who can curtail their catalyst synthesis procedure to maximize efficiency, time, and profit while minimizing the waste of precious, nonrenewable resources. A synthesis procedure capable of synthesizing supported catalysts with controllable and uniform particle size will be investigated in order to attain these goals.

1.6 References

[1] M. Campanati, G. Fornasari, A. Vaccari, *Catalysis Today* 77 (2003) 299.

[2] C.-J. Yang, *Energy Policy* 37 (2009) 1805.

[3] J.H. Sinfelt, Bimetallic Catalysts: Discoveries, Concepts, and Applications. Wiley, New York, 1983.

[4] J.G. Chen, C.A. Menning, M.B. Zellner, *Surface Science Reports* 63 (2008) 201.

[5] B. Hammer, J.K. Nørskov, *Advances in Catalysis* 45 (2000) 71.

[6] J.R. Kitchin, N.A. Khan, M.A. Barteau, J.G. Chen, B. Yahskinskiy, T.E. Madey, *Surface Science* 544 (2003) 298.

[7] H.H. Hwu, J. J. Eng, J.G. Chen, *Journal of the American Chemical Society* 124 (2002) 702.

[8] J.R. Kitchin, J.K. Nørskov, M.A. Barteau, J.G. Chen, *Journal of Chemical Physics* 120 (2004) 10240.

[9] C.A. Menning, H.H. Hwu, J.G. Chen, *Journal of Physical Chemistry B* 110 (2006) 15471.

[10] C.A. Menning, J.G. Chen, *Journal of Chemical Physics* 128 (2008) 164703.

[11] M.P. Humbert, J.G. Chen, *Journal of Catalysis* 257 (2008) 297.

[12] C.A. Menning, J.G. Chen, *Journal of Power Sources* 195 (2010) 3140.

[13] N.A. Khan, M.B. Zellner, J.G. Chen, *Surface Science* 556 (2004) 87.

[14] O. Skoplyak, C.A. Menning, M.A. Barteau, J.G. Chen, *Topics in Catalysis* 51 (2008) 49.

[15] W.W. Lonergan, D.G. Vlachos, J.G. Chen, *Journal of Catalysis* 271 (2010) 239.

[16] R.A.V. Santen, *Accounts of Chemical Research* 42 (2009) 57.

[17] R.V. Hardeveld, A.V. Montfoort, *Surface Science* 4 (1966) 396.

[18] S. Dahl, A. Logadottir, R.C. Egeberg, J.H. Larsen, I. Chorckendorff, E. Törnqvist, J.K. Nørskov, *Physical Review Letters* 83 (1999) 1814.

[19] B. Hammer, *Physical Review Letters* 83 (1999) 3681.

[20] J. Wei, E. Iglesia, *Journal of Physical Chemistry B* 108 (2004) 4094.

[21] J. Wei, E. Iglesia, *Journal of Physical Chemistry B* 108 (2004) 7253.

[22] T.V.W. Janssens, A. Carlsson, A. Puig-Molina, B.S. Clausen, *Journal of Catalysis* 240 (2006) 108.

[23] C. Perego, P. Villa, *Catalysis Today* 34 (1997) 281.

[24] S.D. Mhlanga, N.J. Coville, *Diamond & Related Materials* 17 (2008) 1489.

Chapter 2

REVERSE MICELLE SYNTHESIS AND CHARACTERIZATION TECHNIQUES

2.1 Introduction to Microemulsions

A microemulsion is a thermodynamically stable, optically clear system of two immiscible liquids. They have a variety of applications such as oil recovery[1], oil removal from contaminated groundwater sites[2], cleaning formulations[3], and, more recently, as templates for the synthesis of polymer dispersions[4] and metal nanoparticles.[5] Surfactants, a wetting agent that lowers the surface tension of a liquid, stabilize droplets of water and encourage uniform droplet size.[6] The internal structure of the microemulsion at a given temperature is dependent upon the concentration of its two components: water and oil. At low oil concentrations in water the microemulsions formed will be droplets of oil. The hydrophobic tails of the surfactant will point inward, bonding with the oil molecules, while the hydrophilic ends will remain bonded to water molecules. If there is a low concentration of water in oil, droplets of water form. The hydrophobic tales of the surfactant will point outward towards the oil molecules. The hydrophilic ends will bond to the water molecules within the microemulsion. These microemulsions are commonly referred to as micelles or reverse micelles depending on whether there are droplets of oil in water or droplets of water in oil, respectively. This system is sensitive to temperature, particularly in the case of non-ionic surfactants. Increasing temperature will destroy

oil droplets while decreasing temperature will destroy water droplets. Between the microemulsion solutions a bicontinuous phase exists.[1]

2.2 Preparation of Nanoparticles Using Microemulsions

The ability to create discrete environments of aqueous solution is what makes microemulsions attractive as a catalyst synthesis method. A certain amount of water-soluble material can be dissolved in the aqueous interiors of these droplets, for example metal precursors. Furthermore, a second microemulsion can be created containing a reducing agent to chemically reduce the metal salts instead of relying on high-temperature treatments in H_2 for reduction. These droplets of water within which metal precursor and reducing agents are dissolved serve as the starting point for supported catalyst synthesis. There are two ways to synthesize supported catalysts using revere micelle microemulsions: mixing two microemulsion solutions, one containing a metal precursor and the other containing a reducing agent, or adding the reducing agent directly to the microemulsion with the precipitating agent. The first method is often preferred due to more uniformity involved in the interaction between the reducing agent and metal precursor.[5]

2.3 Effect of Parameters on Particle Size

2.3.1 Size of Water Droplet

The size of the water droplets can be controlled by the molar ratio of water to surfactant, commonly referred to as the ω parameter. Hoefelmeyer et al. found that increasing ω from 2 to 20 yielded micelle diameters ranging from 6.2 to 19.0 nm.[7] Lisiecki and Pileni found that they were able to control the size of copper (Cu) nanoparticles from 2 to 10 nm by increasing ω from 1 to 10.[8] Lee et al. found that

when synthesizing Fe nanoparticles they were able to control the size from 2.92 to 8.95 nm by increasing ω from 3.6 to 8.1.[9] These are three of many sources that illustrate the success of synthesizing metallic nanoparticles using revere micelle synthesis and the control over particle size that the method offers.

2.3.2 Surfactant Concentration

The water droplet size is also affected by the surfactant concentration when the amount of water and oil is kept constant. An increasing amount of surfactant will increase the number of droplets, thus decreasing the size of the particles. Studies have shown that while droplet size influences the size of the particles formed after reduction, final particle size is not directly correlated with droplet size. In the case of Pt particles, a study was performed with $PtCl_6^{2-}$ ions in a microemulsion of pentaethyleneglycol dodecylether surfactant, hexane and water. The concentration was 1.55×10^{20} ions/dm^3. Each droplet was estimated to contain 5 ions; however, TEM analysis of the reduced particles revealed an average size of 3.5 nm, which corresponds to 100-1500 atoms.[5] This suggests that the nucleus of the particle is formed in the droplet, not the particle itself. Since the microemulsion system is dynamic, micelles are constantly colliding and coalescing, allowing aggregation to occur to form the final particle. The rate of particle growth is hindered by the presence of the surfactant which prevents the nuclei from growing too quickly. The particles will then grow at the same rate, producing particles with narrow distribution.[5]

2.3.3 Reducing Agent

The rate at which nanoparticles grow is a function of the reducing agent. Popular reducing agents are hydrazine (N_2H_4) and sodium borohydride ($NaBH_4$), the

former being preferred due to non-contaminating byproducts of N_2 and H_2 during synthesis. Generally, fast nucleation will result in smaller particles. As explained before, the formation of the nucleus in the particle is crucial for uniform particle growth. If nucleation is slow, atoms will collide with nuclei already formed instead of forming a new nucleus. This leads to larger particles. Higher concentrations of reducing agent encourage faster initial formation of nuclei and fewer atoms to collide and increase particle size. For this reason, syntheses are performed with the reducing agent in stoichiometric molar excess to the concentration of metal. Chen and Wu found that the concentration of reductant N_2H_4 and precursor nickel chloride affected particle size differently, depending on the respective ratios. They explained this by the reduction, nucleation and growth processes.[10]

2.4 Preparation of Supported Catalysts from Microemulsions

Microemulsions containing nanoparticles are very stable suspensions, so it is a challenge to separate the particles from the constituents, particularly the surfactants, as its molecules strongly adsorb to the metal nanoparticles. It is necessary to maintain the homogeneous distribution when transferring particles to the support. Reduced particles must adhere strongly to the support to minimize sintering during high-temperature treatments.

The most common way to remove nanoparticles from microemulsions and adhere them to a support is to add a solvent like tetrahydrofuran (THF) or acetone to the microemulsion which will destabilize the surfactants. THF and acetone will compete with surfactant molecules adsorbed onto the particle and displace them, resulting in an unstable suspension. Particles will adhere to the support if it is added during the addition of THF or acetone. This is not always a straightforward task; the

adsorption can depend on the composition of solution, pH, and properties of the support. Just as the factors surrounding nanoparticle formation in microemulsions are plentiful, there are many different reverse micelle synthesis chemistries and procedures reported in the literature.

2.5 Previous Research on Catalyst Synthesis Using Microemulsions

The amount of literature available for catalyst synthesis from microemulsions is staggering. Many research is based off of the work of Boutonnet et al. in 1982 where they synthesized monodisperse Pt, palladium (Pd), rhodium (Rh) and iridium (Ir) particles ranging from 3-5 nm.[11] Since then, many nanoparticles have been synthesized from a wide range of reverse micelle chemistries, which is a result of the large parameter space associated with reverse micelle synthesis. The variables include, but are not limited to, metal precursor, reducing agent, oil phase, surfactant, co-surfactant, volume fractions of the previously-mentioned components, ratios of one of the previously-mentioned components to another, synthesis temperature, stir time, pH of solution, dispersing agent to break micelles, support, and cleaning treatments to remove residual surfactant molecules. An example of the effect of these parameters on particle size is shown in **Table 2.1**.[5]

Table 2.1 Influence of several parameters on the particle size of Pd-based catalysts prepared by different techniques. Abbreviations are pentaethyleneglycol dodecyl ether (PEGDE), poly(oxyethylene)$_5$ (NP-5), dioctyl sodium sulfosuccinate (AOT), Ethoxylated iso-tridecanoles containing 4 moles of ethylene oxide per mole of alcohol (Marlipal O13/40).

Metal precursor	Particle size (nm)	Surfactant	Oil phase	Reducing agent	Preparation method	Reference
$PdCl_2$	5	PEGDE	Hexane	N_2H_4	ME	[11]
$PdCl_2$	6-7	NP-5	Cyclohexane	N_2H_4	ME	[12]
	12				IM	
$Pd(NH_3)_4$	5-8	AOT	*iso*-Octane	N_2H_4	ME	[13]
K_2PdCl_4	2.4-3.8	AOT	*n*-Heptane	N_2H_4	ME	[14]
$PdCl_2$	5	AOT	*iso*-Octane	N_2H_4	ME	[15]
$PdCl_2$	3-10	NP-5	Cyclohexane	N_2H_4	ME	[16]
	12				IM	
$PdCl_2$	5	Marlipal O13/40	Cyclohexane	NaH_2PO_2	ME	[17]
	3 and 11[a]				HM	

ME, microemulsion; IM, impregnation; HM, homogeneous aqueous solution
[a] Bimodal particle size distribution

Each of the research groups featured in **Table 2.1** has its own recipe that they have spent an unknown time optimizing for their particular system. What parameters and treatments may work for one synthesized supported catalyst may not necessarily work for another. While many review articles exist to summarize the recent work done on microemulsions, the tables therein cover a broad range of metals and supports.[5, 11, 18] **Table 2.2** is a more centralized review of work performed with Group VIII metals (Fe, Co, Ni, Ru, Rh, Pd, Pt) since Pt, Co and Ni are the main focus of this thesis.

Table 2.2 Survey of microemulsion-based synthesis of catalytic systems for precious metals and group VIII metals. Microemulsion is surfactant/co-surfactant (if present)/oil phase. Abbreviations are polyoxyethylene ($C_{14}H_{22}O(C_2H_4O)_n$, n~9.5) (Triton X-100); polyoxyethylene (4) lauryl ether (Brij-30), Sodium bis(2-ethylhexyl) sulfosuccinate ($C_{20}H_{37}NaO_7S$) (AOT), cetyltrimethylammonium bromide (CTAB), sodium dodecylbenzenesulfonate (NaDBS), nonylphenolethoxylate (NP-5).

Catalyst	Metal precursor	Reductant	Microemulsion	Use	Ref.
Ni	$NiCl_2$	N_2H_4	CTAB/*n*-hexanol	Broad	[10]
Co	$Co(CH_3CO_2)_2$	$NaBH_4$	AOT,lauric acid/ isooctane,hexane	Magnetic nanocrystals	[19]
Co/SiO_2	$Co(NO_3)_2$	N_2H_4	AOT & Triton X-100/*n*-hexanol	Fischer-Tropsch	[20]
$Fe/CaCO_3$	$FeCl_2$ $Fe(NO_3)_3$	N_2H_4	NaDBS/xylene	Broad (magnetic)	[9]
Rh	Na_3RhCl_6	$NaBH_4$	Lauric acid & butyl amine/hexanes	Tune properties	[7]
$Pd/\gamma\text{-}Al_2O_3$	$Pd(NO_3)_2$	N_2H_4	NP-5/cyclohexane	Methane oxidation	[21]
$Pt/\gamma\text{-}Al_2O_3$ $Ni/\gamma\text{-}Al_2O_3$ $PtNi/\gamma\text{-}Al_2O_3$	$Pt(NH_3)_2(NO_2)_2$, $Ni(NO_3)_2$	N_2H_4	Triton X-100/ 1-propanol/ cyclohexane	Methane reforming	[22]
PtCo/C	H_2PtCl_6 $CoCl_2$	N_2H_4	Triton X-100/ 2-propanol/ cyclohexane	Formic acid oxidation	[23]
$PtPd/\gamma\text{-}Al_2O_3$	$PtCl_4$ $PdCl_2$	N_2H_4	Brij-30/ hexadecane	CO oxidation	[24]
PtRu/C	H_2PtCl_6 $RuCl_3$	$NaBH_4$	AOT/ cyclohexane	Methanol oxidation	[25]
Pt/C PtRu/C	H_2PtCl_6, $Ru(NO)(NO_3)_3$	N_2H_4	Berol 050/ isooctane	Methanol oxidation	[5]

After synthesis of supported catalysts, many methods are available to characterize catalysts to help understand nanoparticle size, shape, extent of bonding between metal atoms, and active sites available for chemical reactions. The techniques used in this thesis to evaluate catalysts are described briefly in the next section.

2.6 Catalyst Characterization Techniques

Many characterization techniques were utilized to determine the physical and chemical properties of the synthesized catalysts. Among these were transmission electron microscopy (TEM) to determine particle size, extended X-ray absorption fine structure (EXAFS) spectroscopy to determine interatomic distances and coordination numbers to indicate bimetallic bond formation, and atomic absorption spectroscopy (AAS) to determine metal loading. Other techniques probed catalytic activity, including pulse carbon monoxide (CO) chemisorption to determine active sites, and *in situ* Fourier transform infrared (FTIR) spectroscopy to monitor products and reactants during hydrogenation to determine catalytic activity.

2.6.1 Pulse CO Chemisorption

An AMI-200ip (Altamira Instruments) was used to perform pulse chemisorption to determine CO uptake and metal dispersion. Approximately 0.1 g of catalyst was loaded into a quartz U-tube with quartz wool to hold it in place. Catalysts were reduced at 723 K for 1 hour in a 50 sccm of a 50% hydrogen/helium (H_2/He) mixture. Once the catalyst was cooled to room temperature in He, pulse CO chemisorption was performed using 58 µl pulses of CO in He carrier gas. CO uptake in µmol CO per gram of catalyst was calculated with the integrated analytical area

from chemisorption and the calibration of 58 µl pulses of 100% CO in He carrier gas. Metal dispersion was calculated from CO uptake assuming a stoichiometry of M:CO = 1:1, where M = Pt, Ni, Co. Due to the estimation of stoichiometry, dispersion values may not be accurate, but will be reported as a relative ranking metal dispersion. The amount of adsorbed CO provides a quantitative comparison of the number of active sites, which can be correlated with reaction activity.

2.6.2 Transmission Electron Microscopy (TEM)

Particle size distributions were determined using JEM-2000FX and 2010F electron microscopes operating at 200 kV with an ultra-high resolution pole piece providing point resolution of 0.29 nm and 0.19, respectively. High angle annular dark field (HAADF) images were collected on the JEM-2010F with a camera length of 20 cm and a probe size of 0.5 nm HR. Bright field images were collected on the JEM-2000FX.

To image micellar solutions, 2 drops of micellar solution containing reduced nanoparticles before supporting were placed on a Lacey carbon film supported on a 200-mesh copper grid (Electron Microscopy Sciences). The grid was washed with five drops of acetone to ensure removal of surfactant, and then dried in air. Supported catalysts were pre-treated in H_2 at 723 K for 1 hour before TEM analysis. To image supported catalyst samples, catalyst powders were dispersed in ethanol and 2 drops of the solution were transferred to grids. Grids were allowed to dry overnight before TEM characterization.

2.6.3 Fourier Transform Infrared (FTIR) Spectroscopy

FTIR spectroscopy was used to monitor the products and reactants of hydrogenation reactions to determine catalytic activity. Batch reactor studies of benzene and 1,3-butadiene hydrogenation were performed to determine whether catalysts synthesized using reverse micelles exhibited activity comparable to or better than incipient wetness impregnated catalysts, and to determine whether bimetallic catalysts exhibited increased reaction rates as compared to the corresponding monometallic catalyst. 25 mg of powder catalyst were pressed onto rectangular tungsten mesh (Alfa Aesar) with spot-welded alumel and chromel thermocouple wires to monitor temperature while the catalyst was resistively heated to desired temperatures. Catalysts were reduced in 30 Torr H_2 at 723 K for 30 minutes. Following evacuation and cooling to room temperature, the sample was rapidly resistively flashed to 723 K to remove any surface species generated during reduction. This reduction-flash cycle was repeated 3 times.

Spectra were recorded every 30 seconds averaging 32 scans per spectrum with 4 cm^{-1} resolution using a Nicolet-470 FTIR spectrometer equipped with a mercury cadmium telluride (MCT) detector. By integrating the peak height over time and monitoring the peak height of each vibrational mode as a function of the pressure, the concentration over time could be monitored for reactants and products.

For benzene hydrogenation, H_2 was added in a 4:1 stoichiometric ratio to benzene. 3 Torr of benzene, 12 Torr of H_2 and 15 Torr of He were added to the chamber and allowed to react for 4 hours. For data analysis, the concentrations of the two main gas-phase species, benzene and cyclohexane were estimated using the peak heights of their vibrational modes at 1810 cm^{-1} (overtone of the C-C stretching mode at 993 cm^{-1}) and 1458 cm^{-1} (-CH_2 deformation), respectively. The peak height at 1139

cm^{-1} (ωCH_2 vibrational mode), characteristic of cyclohexene, was also monitored, but did not appear in any reactions. Concentration calibrations were performed by W.W. Lonergan. A sample spectrum containing peaks characteristic of the reactants and products is shown in **Figure 2.1**.

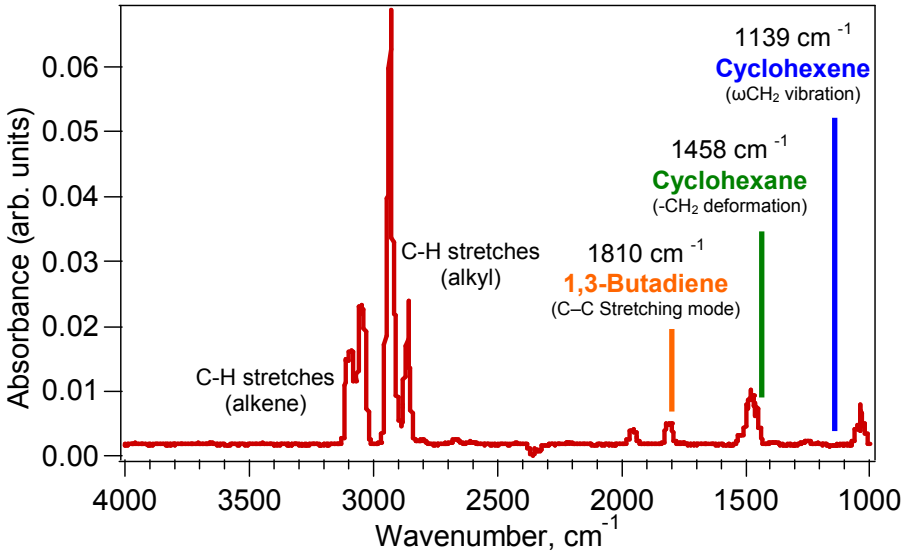

Figure 2.1 Characteristic spectrum for reactant benzene and product cyclohexane in benzene hydrogenation. Cyclohexene was not observed during reaction.

For 1,3-butadiene hydrogenation, H_2 was added in a 2.2:1 stoichiometric ratio to 1,3-butadiene. 2.5 Torr of 1,3-butadiene, 5.5 Torr of H_2 and 30.1 Torr of He were added to the chamber and allowed to react for 3 hours. The concentrations of 1,3-butadiene, 1-butene and n-butane were monitored using the intensities of the characteristic vibrational modes at 1586 cm^{-1} (C=C-C=C deformation), 1655 cm^{-1}

(C=C deformation), and 1466 cm^{-1} (CH_2 deformation), respectively. Since both 1-butene and n-butane contain CH_2 deformation, the intensity at 1466 cm^{-1} that pertained to 1-butene was subtracted form that of n-butane. This was determined based on the ratio of the peak at 1466 cm^{-1} to that of 1655 cm^{-1}. The equation used is listed below where *I* is peak intensity and *C* is measured concentration.

$$I_{Bu\tan e(1466)} = I_{Total(1466)} - C_{1-Butene(1655)}\left(\frac{I_{1-Butene(1466)}}{C_{1-Butene(1466)}}\right) \quad \textbf{(2.1)}$$

Concentration calibrations were performed by W.W. Lonergan. A sample spectrum containing peaks characteristic of the reactants and products is shown in **Figure 2.2**.

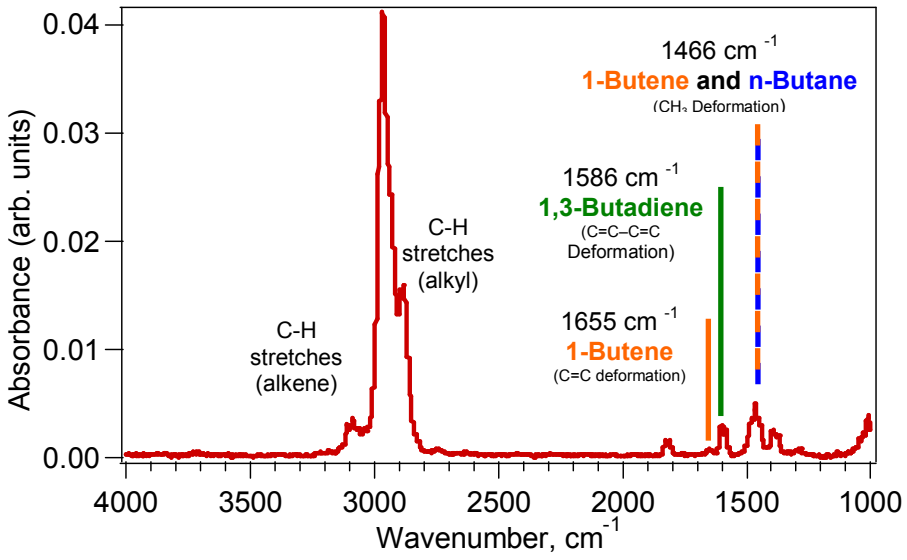

Figure 2.2 Characteristic spectrum for reactant 1,3-butadiene and products 1-butene and n-butane in 1,3-butadiene hydrogenation.

2.6.4 Extended X-ray Absorption Fine Structure (EXAFS) Spectroscopy

EXAFS measurements were performed at the National Synchrotron Light Source (NSLS) in Brookhaven National Laboratory on the X18B and X19A beamlines to determine the nearest-neighbor coordination numbers and interatomic distances in order to determine the presence of Pt-Co and Pt-Ni bimetallic bonds. Catalyst powder was pressed into pellets using a force of approximately 3.5 tons/cm^2. Catalyst mass was chosen so that samples would be have a thickness on the order of two absorption coefficients. This optimizes the signal to noise ratio. Pellets were loaded into EXAFS cell which allows for *in situ* reduction and collection of transmission and fluorescence signals. The sample was heated to 723 K at a rate of 14 K/min under 5% H_2 in He (40 sccm) and reduced for 1 hour before cooling to room temperature. Scans near and above the Pt L_{III}-edge were collected at room temperature before and after reduction using a double crystal Si(111) monochromator. The incident and transmitted x-rays were measured with ionization chambers and a germanium detector was used to collect the fluorescence signal. EXAFS measurements on a Pt foil were performed in transmission mode for the edge calibration.

Data collection occurred in three energy regions: the pre-edge region was scanned every 5 eV from -150 to -25 eV before the edge, the near-edge region was scanned every 0.5 eV from -25 eV before the edge to 40 eV past the edge, and the post-edge region was scanned every 0.05k (approximately 3 eV) from 40 eV to 18k (approximately 1450 eV) past the edge. The integration times for each region were 1 second, 2 seconds, and 2 seconds, respectively. The IFFEFIT 1.2.9 data analysis package (Athena, Artemis, Atoms and FEFF6) was used to analyze data and fit the first nearest neighbor shell.[26, 27]

Data was imported into Athena as $\ln(I_o/I_t)$ for transmission data or the (sum of the fluorescence signals from a 12-channel germanium detector)/I_o, where I_o is the initial X-ray intensity and I_t is the transmitted X-ray intensity after the absorption from the sample. A reference scan was collected with each scan and was imported into Athena as $\ln(I_t/I_{ref})$, where I_{ref} is the transmitted X-ray intensity after the absorption from the reference Pt foil. Data reduction consisted of calibrating each reference scan to the Pt L_{III}-edge energy of 11,564 eV. The data was then aligned to the foil standard and deglitched, if necessary. The multiple scans collected for each edge were then merged to reduce experimental error and then the AUTOBK algorithm in Athena was used to remove the isolated-atom background function from the EXAFS data. The EXAFS signal was then Fourier-transformed into R-space and Artemis was used to obtain local structural information for the first coordination shell. The Pt L_{III}-edges were modeled by including both Pt–Pt and Pt–3*d* (Co or Ni) contributions in the theoretical EXAFS generated using FEFF6. The Pt–Pt theoretical photoelectron scattering-path amplitudes and phases were calculated for the bulk Pt fcc structure. Pt–3*d* contributions were modeled in FEFF6 by using the Pt face-centered cubic (fcc) structure with the exception that the Pt atoms in the first nearest-neighbor shell were replaced with the appropriate 3*d* metal atom. The seven variables used in the fitting procedure were the coordination numbers of Pt–Pt and Pt–3*d* bonds, two corrections to the model interatomic distances, two EXAFS Debye–Waller factors (mean-square deviations in interatomic distances), and the correction to the photoelectron energy. By fitting the Pt reference foil, the passive electron reduction factor, $S_0^2 = 0.85$ was determined, and this value was held fixed in the analysis of the bimetallic catalysts.

2.6.5 Atomic Absorption Spectroscopy (AAS)

AAS was used to determine the weight loadings of supported catalysts using the SOLAAR S Series spectrometer from Thermo Elemental. The principal of AAS involves the absorption by free atoms of an element of light at a wavelength specific to that element. The light source was provided by hollow cathode lamps purchased from Thermo Elemental**. Table 2.3** contains information regarding the preparation of catalysts for the detection of Pt and Ni.

Table 2.3 Preparation details for atomic absorption spectroscopy analysis of supported Pt-Ni catalysts.

Metal	Wt%	Wavelength (nm)	Desired ppm	Amount needed for 50 ml (g)	Digestion solution	Matrix solution
Pt	1.67	232	30	0.09	4 ml HNO_3, 12 ml HCl	10% HCl
Ni	1.50	266	100	0.33	8 ml HNO_3, 8 ml HCl	4% HNO_3

Catalysts were mixed in the digestion solutions overnight. Solutions were heated gently and carefully while mixing until about 5 ml of solution remained in the vial. Solutions were then diluted to 50 ml with the corresponding matrix solution. The sample solution was burned in a flame fueled by an air and acetylene, the ratio of which was optimized for the metal of interest. The absorbance for incipient wetness catalysts was used to normalize the absorbance for reverse micelle catalysts in order to make a comparison between metal uptake of catalysts prepared using both synthesis techniques.

2.7 References

[1] M. Schwuger, K. Stickdorn, *Chemical Reviews* **95** (1995) 849.

[2] C.C. West, J.H. Harwell, *Environmental Science and Technology* **26** (1992) 2324.

[3] J. Mihelic, L.B. Luttinger, *US Patent 5 401 326* (1995).

[4] W.F.C. Sager, *Current Opinion in Colloid Interface Science* **3** (1998) 276.

[5] S. Eriksson, U. Nylén, S. Rojas, M. Boutonnet, *Applied Catalysis A: General* **265** (2004) 207.

[6] J. Klier, C.J. Tucker, T.H. Kalantar, D.P. Green, *Advanced Materials* **12** (2000) 1751.

[7] J.D. Hoefelmeyer, H. Liu, G.A. Somorjai, T.D. Tilley, *Journal of Colloid and Interface Science* **308** (2006) 86.

[8] I. Lisiecki, M.P. Pileni, *Journal of American Chemical Society* **115** (1992) 3887.

[9] Y. Lee, J. Lee, C.J. Bae, J.-G. Park, H.-J. Noh, J.-H. Park, T. Hyeon, *Advanced Functional Materials* **15** (2005) 503.

[10] D.-H. Chen, S.-H. Wu, *Chemical Materials* **12** (2000) 1354.

[11] M. Boutonnet, J. Kizling, P. Stenius, G. Maire, *Colloids and Surfaces* **5** (1982) 209.

[12] M. Kishida, K. Umakoshi, J. Ishiyama, H. Nagata, K. Wakabayashi, *Journal of the Chemical Society, Chemical Communications* **7** (1996) 763.

[13] W.Y. Kim, T. Hanaoka, M. Kishida, K. Wakabayashi, *Applied Catalysis A: General* **155** (1997) 283.

[14] B.H. Robinson, A.N. Khan-Lodhi, T. Towey, Structure and Reactivity in Reverse Micelles. Elsevier, Amsterdam, 1989, 198.

[15] M.-L. Wu, D.-H. Chen, T.-C. Huang, *Journal of Colloid and Interface Science* **243** (2001) 102.

[16] J. Agrell, M. Boutonnet, U. Jacobsson, J.C. Eriksson, *Unpublished results from 1999*.

[17] M. Lade, H. Mays, J. Schmidt, R. Willumeit, R. Schomäcker, *Colloids and Surfaces A: Physiochemical and Engineering Aspects* **163** (2000) 3.

[18] M. Boutonnet, S. Lögdberg, E.E. Svensson, *Current Opinion in Colloid and Interface Science* **13** (2008) 270.

[19] I. Lisiecki, M.P. Pileni, *Langmuir* **19** (2003) 9486.

[20] A. Martínez, G. Prieto, *Catalysis Communications* **8** (2007) 147901486.

[21] K. Persson, P.O. Thevenin, K. Jansson, J. Agrell, S.G. Järås, L.J. Pettersson, *Applied Catalysis A: General* **249** (2003) 165.

[22] M. García-Diéguez, I.S. Pieta, M.C. Hererra, M.A. Larrubia, L.J. Alemany, *Applied Catalysis A: General* **377** (2010) 191.

[23] X. Zhang, K.-Y. Tsang, K.-Y. Chan, *Journal of Electroanalytical Chemistry* **573** (2004) 1.

[24] M. Yashima, L.K.L. Falk, A.E.C. Palmqvist, K. Holmberg, *Journal of Colloid and Interface Science* **268** (2003) 348.

[25] Y. Liu, X. Qiu, Z. Chen, W. Zhu, *Electrochemistry Communications* **4** (2002) 550.

[26] M. Newville, *Journal of Synchrotron Radiation* **8** (2001) 96.

[27] M. Newville, B. Ravel, *Journal of Synchrotron Radiation* **12** (2005) 537.

Chapter 3

SYNTHESIS AND CHARACTERIZATION OF SUPPORTED CATALYSTS CONTAINING PLATINUM AND COBALT

3.1 Applications of Platinum-Cobalt Catalysts

Pt-based bimetallic catalysts exhibit enhanced activity and selectivity when alloyed with another metal. Research performed by the Chen group has shown that model systems of Pt-Ni-Pt(111) and Pt-Co-Pt(111) show higher activity for low-temperature hydrogenation.[1] Studies performed on supported catalysts confirmed that Pt-Co and Pt-Ni bimetallic catalysts supported on γ-Al_2O_3 exhibited significantly higher benzene hydrogenation activity than monometallic catalysts.[2] This increase in activity is attributed to shift in surface *d*-band center from DFT calculations which affect adsorbate binding energies.[3]

Exploratory research with reverse micelle synthesis was performed by the Lauterbach group with Pt and Co adsorbed onto a barium (Ba)-impregnated γ-Al_2O_3 powder. Rohit Vijay's doctoral work focused on NO_x storage reduction (NSR) and found that Co had a large promotional effect on the NSR activity of traditional Pt/Ba catalysts. This led to a reduction of noble metal without affecting the performance.[4] Vijay found that a 0.25 wt% Pt / 1.25 wt% Co catalyst supported on 15% Ba-impregnated γ-Al_2O_3 had the same NO_x storage has a 1.0 wt% Pt catalyst supported on 15% Ba-impregnated γ-Al_2O_3. Using reverse micelle synthesis he was able to synthesize small (~ 5 nm) nanoparticles whose compositions closely matched those of

the desired metal loadings.[5] Given the intersection of previous work performed on Pt-Co bimetallic supported catalysts in the Chen group and reverse micelle synthesis in the Lauterbach group, this system of metals was chosen as a starting point for optimizing reverse micelle synthesis.

3.2 Reverse Micelle Synthesis

Two aqueous solutions were mixed: the first was a metal precursor solution made by dissolving chloroplatinic acid hexahydrate (H_2PtCl_6-$6H_2O$, Sigma Aldrich) and cobalt (II) nitrate hexahydrate ($Co(NO_3)_2$-$6H_2O$, Strem Chemicals) in DI water and the second was a reductant solution made by dissolving solid sodium borohydride ($NaBH_4$, Sigma Aldrich) in DI water. The amount of metal salt required was dictated by the desired catalyst mass and desired Pt/Co ratio. The amount of water in the metal salt solution was calculated by setting the concentration of metal in water to 0.10 M. The amount of reductant corresponded to a reductant to metal molar ratio of 15. Micelle solutions were made for each aqueous solution consisting of a 0.10 M solutions of surfactant polyoxyethylene (4) lauryl ether (Brij-30, Sigma Aldrich) in cyclohexane (Fisher Scientific). The ω parameter, $[H_2O]$ / [Brij-30], was 3.0. A table containing the values used for measuring enough solvents to synthesize 0.30 grams of 1.0 wt% Pt / 5.0 wt% Co /γ-Al_2O_3 is shown in **Table 3.1**.

Table 3.1 Synthesis parameters used to synthesize 0.30 grams of 1.0 wt% Pt / 5.0 wt% Ni /γ-Al_2O_3. Gray cells indicate that the value is adjustable.

Defined Parameters	
Parameter	Value
[M] in H_2O (mol/L)	0.10
[$NaBH_4$] (mol/L)	1.50
[Brij-30] in Cyclohexane	0.10
Omega, ω	3.0

Determined by Catalyst	
Parameter	Value
Amount of Catalyst (g)	0.30
Wt % Pt	1.0%
Wt % Co	5.0%
γ-Al_2O_3 (g)	0.28

Measured for Catalyst Synthesis		
Component	Beaker 1	Beaker 2
H_2PtCl_6-$6H_2O$ (g)	0.01	--
$Co(NO_3)_2$-$6H_2O$ (g)	0.07	
Water (ml)	2.70	2.70
Brij-30 (ml)	19.06	19.06
Cyclohexane (ml)	499.4	499.4
$NaBH_4$ (g)	--	0.153
Total volume (ml)	1042	
Volume acetone (ml)	2085	

Aqueous solutions of metal or reductant and water were added to micelle solutions of Brij-30 and cyclohexane ([Brij-30] in cyclohexane = 0.10 M) under vigorous stirring until optical clarity was reached, indicating the formation of reverse micelles. The reductant solution was added quickly to the metal solution and the observed change in color (orange to black for Pt metal salt) indicated a complete reduction reaction. After stirring overnight, the γ-Al_2O_3 powder support (Catalox® Sba-200, 200 m^2/g) was added simultaneously as the solution was titrated with acetone to disrupt the micelles and precipitate the nanoparticles onto the support. The solution

was filtered and rinsed copiously with acetone to remove surfactant from supported particles. Catalysts were heated prior to characterization in order to remove residual surfactant. Pre-treatment involved heating to 473 K in O_2 (Keen) for 2 hours, holding for 1 hour at 473 K, followed by a 3 hour ramp to 823 K and a subsequent 2 hour hold. Catalysts were then cooled to room temperature before characterization.

3.3 Incipient Wetness Impregnation

As a reference for comparison between synthesis techniques, comparison with a monometallic 1.7%Pt/γ-Al_2O_3 catalyst that had been previously synthesized and characterized will be made. Research in literature showed that a chlorinated Pt precursor (H_2PtCl_6-$6H_2O$ - the precursor for these reverse micelle catalysts) affects reactivity of catalysts synthesized by incipient wetness impregnation on γ-Al_2O_3. In one study, residual chlorine (Cl) remained on the surface of Pt/γ-Al_2O_3 catalyst and inhibited *o*-xylene hydrogenation; however, Cl promoted the *cis*-to-*trans* configurational isomerization reaction.[6] It is expected that Pt will exist only in its reduced state after chemical reduction in reverse micelle synthesis and Cl should remain in solution and not adhere to the support. Since incipient wetness impregnation involves impregnating the metal ion from precursor, calcining, and reducing in H_2 to produce metallic nanoparticles, it is more likely that Cl would remain on the support surface. Comparisons were therefore made with a 1.7%Pt/γ-Al_2O_3 catalyst synthesized with $Pt(NH_3)_4(NO_3)_2$ (Alfa Aesar) instead of H_2PtCl_6-$6H_2O$. This precursor has been used often within the Chen group and its properties and pre-treatments were well-established. The precursor was dissolved in DI water, the volume of which was equivalent to the pore volume of the support and impregnated onto the support γ-Al_2O_3 (Alfa Aesar, 80-120 m^2/g). After impregnation,

catalyst was dried in air at 373 K for 10 hours and calcined at 563 K for 3 hours to decompose the salts.

3.4 Catalyst Characterization

3.4.1 Analysis of Surface Area Using Pulse CO Chemisorption

Pulse CO chemisorption was used to determine the number of active sites for catalysts. CO uptake per gram of catalyst is listed for each catalyst in **Table 3.2**. Percent dispersions are based on a stoichiometry of M:CO (M = Pt, Co) of 1:1. The percent loading is defined as the combination of all metal percents in the catalyst (for example, 6% for 1%Pt and 5%Co). As a result, the percent dispersions listed may not be physically meaningful, but are listed to give a relative ranking of metal dispersion.

Table 3.2 CO uptake and dispersions for Pt and Pt-Co catalysts.

Catalyst	CO uptake (μmol CO / g catalyst)	CO uptake (μmol CO / g Pt)	Dispersion (%)
0.25%Pt/γ-Al_2O_3	4.9	1960	38.1
0.25%Pt-1.25%Co/γ-Al_2O_3	3.0	1200	3.9
1%Pt/γ-Al_2O_3	12.9	1290	25.2
1%Pt-5%Co/γ-Al_2O_3	1.2	120	0.4
1.7%Pt/γ-Al_2O_3, IW	28.0	1647	32.7

When comparing monometallic Pt catalysts with bimetallic Pt-Co catalysts, the CO uptake decreased. The CO uptake was normalized to the amount of Pt in the catalyst to determine whether alloying with Co had a positive impact on CO uptake. Bimetallic catalysts had lower CO uptake than their corresponding

monometallic catalysts. Unexpectedly, the lowest metal loading 0.25%Pt/γ-Al_2O_3 had the highest CO uptake per gram Pt, even when compared with incipient wetness impregnated 1.7%Pt/γ-Al_2O_3. Particle size determined from TEM shows the number of surface sites available for CO adsorption.

3.4.2 Nanoparticle Size Analysis Using TEM

Particle size statistics, located in **Table 3.3**, were created by measuring horizontal particle diameter in several collected TEM images using high angle annular dark field (HAADF) imaging. Relative standard deviation (RSD) is calculated as the standard deviation ÷ average particle diameter.

Table 3.3 Particle size statistics. *Indicates data from W.W. Lonergan.[7]

Catalyst	Median diameter (nm)	Average diameter (nm)	Standard deviation (nm)	RSD
0.25%Pt/γ-Al_2O_3	7.3	8.3	3.1	37%
0.25%Pt-1.25%Co, Unsupported	4.1	4.0	0.6	15%
0.25%Pt-1.25%Co/γ-Al_2O_3	2.7	2.9	1.0	34%
1%Pt, Unsupported	4.5	4.5	0.9	20%
1%Pt/γ-Al_2O_3	6.2	6.3	1.6	25%
1%Pt-5%Co/γ-Al_2O_3	2.7	3.0	1.2	40%
1.7%Pt/γ-Al_2O_3*	1.4	1.9	1.4	74%

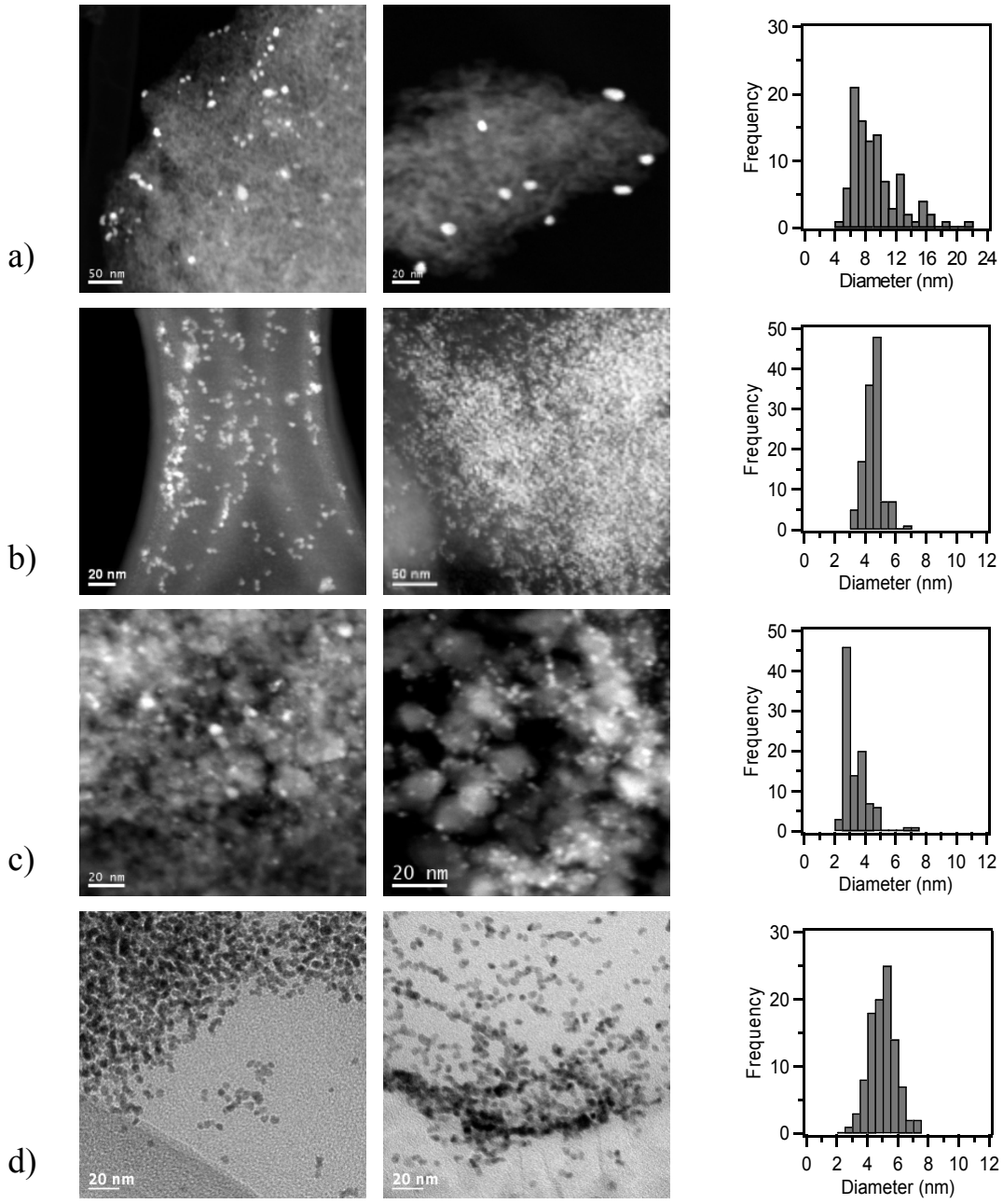
a)
50 nm
20 nm
Frequency
Diameter (nm)
b)
20 nm
50 nm
Frequency
Diameter (nm)
c)
20 nm
20 nm
Frequency
Diameter (nm)
d)
20 nm
20 nm
Frequency
Diameter (nm)

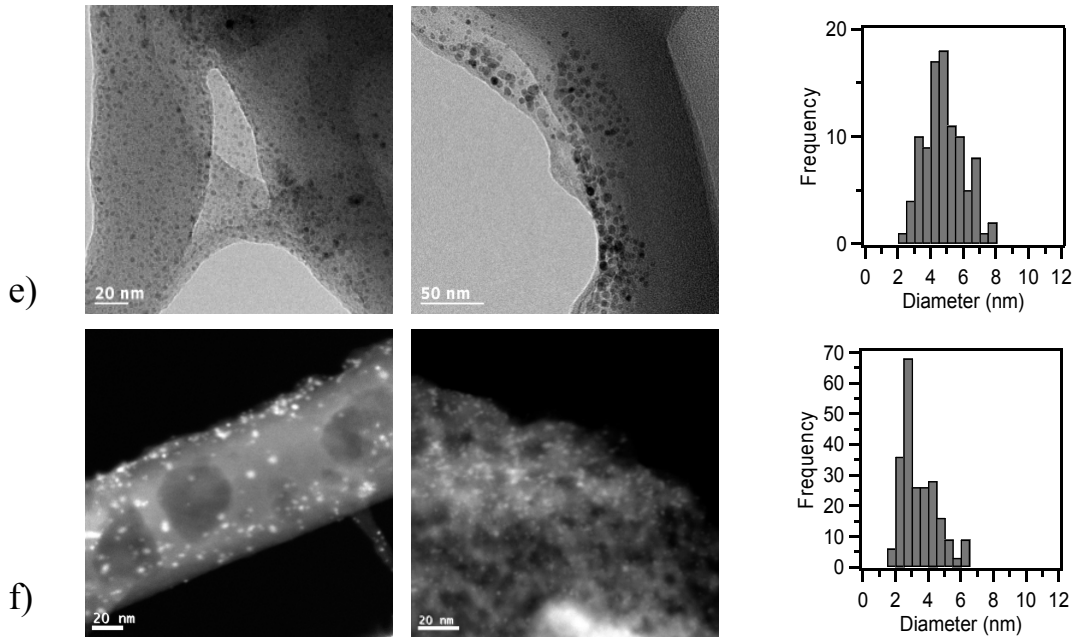

Figure 3.1 HAADF images and bright field images. a) 0.25%Pt/γ-Al_2O_3, b) reduced, unsupported 0.25%Pt/1.25%Co, c) 0.25%Pt/1.25%Co/γ-Al_2O_3, d) reduced, unsupported 1%Pt, e) 1%Pt/γ-Al_2O_3, f) 1%Pt/5%Co/γ-Al_2O_3.

The reduced, unsupported nanoparticles in 0.25%Pt-1.25%Co and 1%Pt have narrow particle size distributions as indicated by an RSD of 15% and 20%, respectively. Upon supporting on γ-Al_2O_3 the particle size distribution ranges from 25% to 40% across all reverse micelle catalysts. The incipient wetness catalyst, 1.7%Pt/γ-Al_2O_3, has the highest relative standard deviation of 74% partially due to its small average diameter. Given that the median is similar to the average diameter, it is statistically relevant that the frequency of smaller particles dominates over the larger particles that were reported (4-10 nm). Agglomerations were not observed in reverse micelle catalysts.

There is a trend of weight loading on average diameter when considering supported catalysts. When total weight loading is increased from 0.25%, 1%, 1.5% (=0.25% + 1.25%), 6% (=1% + 5%) the average diameter decreases from 8.3, 6.3, 2.9, 3.0 nm, respectively. However, ideally within reverse micelle synthesis the particle size should be dependent only on the micelle droplet size and not weight percent. The quantity of solvents is dependent upon metal loading and therefore mass transfer effects could affect particle size. The same synthesis technique should be consistent between catalysts regardless of weight loading, which has been demonstrated in the literature for reduced, unsupported Pt-Co nanoparticles synthesized by reverse micelle synthesis.[8]

3.4.3 Benzene Hydrogenation Activity Analysis Using FTIR Spectroscopy

The concentrations of benzene, cyclohexane and cyclohexene were monitored during benzene hydrogenation to determine reaction rates for supported, calcined Pt and Pt-Co catalysts. A gas-phase carbon balance was performed to ensure all products and reactants were accounted for. No cyclohexene was produced during the reaction. Benzene and cyclohexane concentrations are displayed in **Figure 3.2**. Rate constants were determined assuming that benzene hydrogenation was first order, shown in a solid black line in **Figure 3.2,** and are listed in **Table 3.4.**

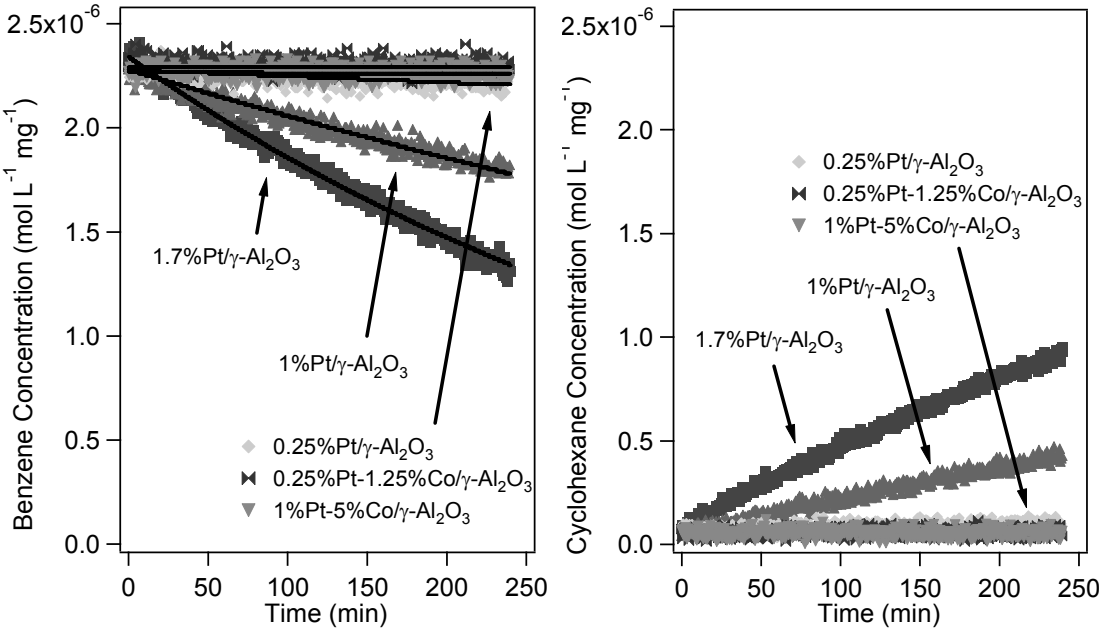

Figure 3.2 Benzene consumption (left) and cyclohexane (right) production during the hydrogenation of benzene at 343 K

Table 3.4 First-order consumption rate constants for hydrogenation of benzene over Pt and Pt-Co catalysts. *Indicates data from W.W. Lonergan.[7]

Catalyst	Benzene k (min^{-1}) x 10^3	CO uptake (μmol CO / g catalyst)	CO uptake (μmol CO / g Pt)	Dispersion (%)
0.25%Pt/γ-Al_2O_3	0.14	4.9	1960	38.1
0.25%Pt-1.25%Co/γ-Al_2O_3	0.00	3.0	1200	3.9
1%Pt/γ-Al_2O_3	0.95	12.9	1290	25.2
1%Pt-5%Co/γ-Al_2O_3	0.02	1.2	120	0.4
1.7%Pt/γ-Al_2O_3*	2.40	28.0	1647	32.7

Both bimetallic catalysts are inactive, which coincides with low CO uptake found during CO pulse chemisorption. A suggestion for low activity could

possibly be the larger Pt:Co atomic ratio of 1:17; however previous research has shown that catalysts supported on γ-Al_2O_3 using incipient wetness impregnation containing 1.2%Pt-10%Co and 1.2%Pt-30%Co catalysts outperformed their corresponding monometallic catalysts. These catalysts correspond to atomic ratios of 1:28 and 1:83, respectively, therefore the Pt:Co atomic ratio of 1:17 cannot be an explanation for low uptake.[2] Given that enhanced activity occurs for catalysts with bimetallic bond formation, EXAFS was used to determine the extent of bimetallic interactions between Pt and Co atoms.

3.4.4 Evaluation of Pt-Co Bimetallic Bond Formation Using EXAFS Spectroscopy

EXAFS and X-ray absorption near-edge structure (XANES) were performed to elucidate the effect of reduction conditions on oxidation state and investigate the extent of bimetallic interactions between Pt and Co atoms. Due to the low metal loading of 1% by weight Pt, fluorescence data was collected by a 12-channel germanium detector. **Figure 3.3 (left)** shows the Pt L_{III}-edge XANES of 1%Pt/γ-Al_2O_3, 0.25%Pt-1.25%Co/γ-Al_2O_3, 1%Pt-5%Co/γ-Al_2O_3 before and after reduction in H_2 and XANES spectrum of Pt foil to serve as a reference for reduced Pt. The spectra shown in **Figure 3.3 (right)** have been treated with background subtraction, edge step normalization and have been k^2-weighted. Data were Fourier-transformed using a *k*-range between 2 $Å^{-1}$ and 16 $Å^{-1}$. The Hanning window function was used with a width of $\Delta k = 2$ $Å^{-1}$.

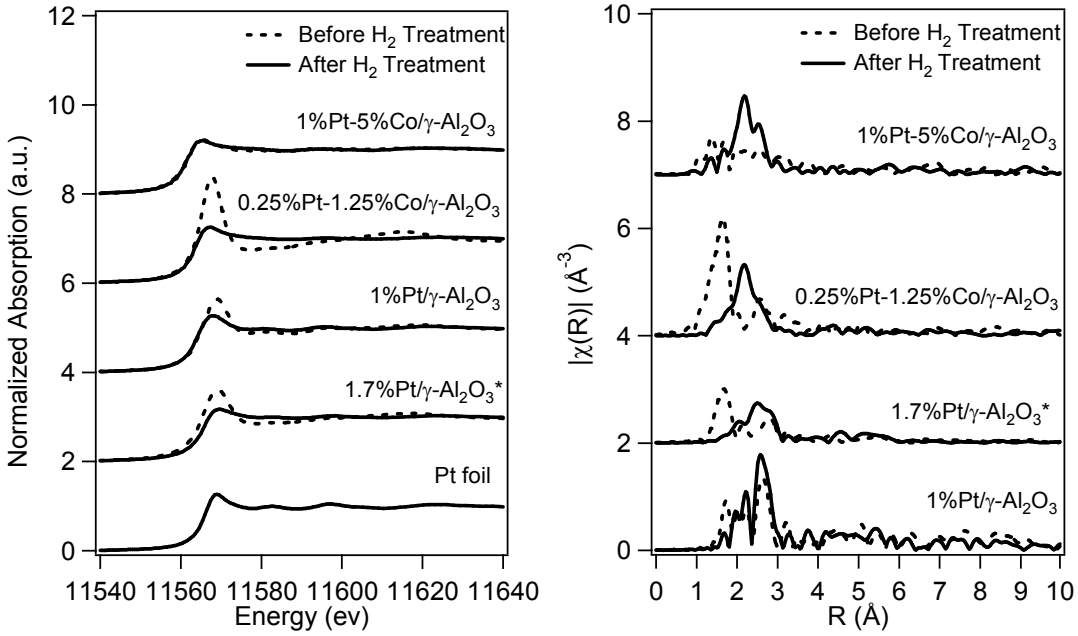

Figure 3.3 Left: Normalized absorption of L_{III}-edge XANES spectrum of 1%Pt-5%Co/γ-Al_2O_3, 0.25%Pt-1.25%Co/ γ-Al_2O_3, and 1%Pt/γ-Al_2O_3 before and after reduction. The Pt foil is included to serve as a reference for reduced Pt XANES spectrum. Right: Fourier-transformed (magnitude) k^2-weighted EXAFS function (χ(k)) of Pt L_{III}-edge of catalysts before and after reduction. *Indicates data from W.W. Lonergan.[7]

The peaks observed at low R-space in **Figure 3.3 (right)** are due to the presence of Pt-O bonds. These peaks are pronounced in 0.25%Pt-1.25%Co/γ-Al_2O_3; however they are not as prominent in 1%Pt/ γ-Al_2O_3 and 1%Pt-5%Co/γ-Al_2O_3. In reverse micelle synthesis the metal is chemically reduced by $NaBH_4$, therefore there should be no Pt-O bonds. It is possible that Pt oxidized in air, resulting in Pt-O bond formation. After reduction in H_2 these peaks disappear, as shown in **Figure 3.3**, where the white line intensity from the catalysts before H_2 reduction decreases to resemble

that of a Pt foil, indicating that the catalysts were reduced. The resulting peaks at larger values of R are due to Pt-Co and Pt-Pt bond interactions. The difference in shape between 1%Pt/γ-Al_2O_3 and the bimetallics 0.25%Pt-1.25%Co/γ-Al_2O_3 and 1%Pt-5%Co/γ-Al_2O_3 indicate that the Pt atoms are altered by the presence of Co. **Figure 3.4** represents the Fourier-transformed experimental data after reduction and the fits obtained used FEFF6 theory. The EXAFS data were fit by incorporating Pt-Pt and Pt-Co interactions. Due to the disappearance of Pt-O peaks in **Figure 3.3 (right)**, Pt-O contributions were not evaluated in the model.

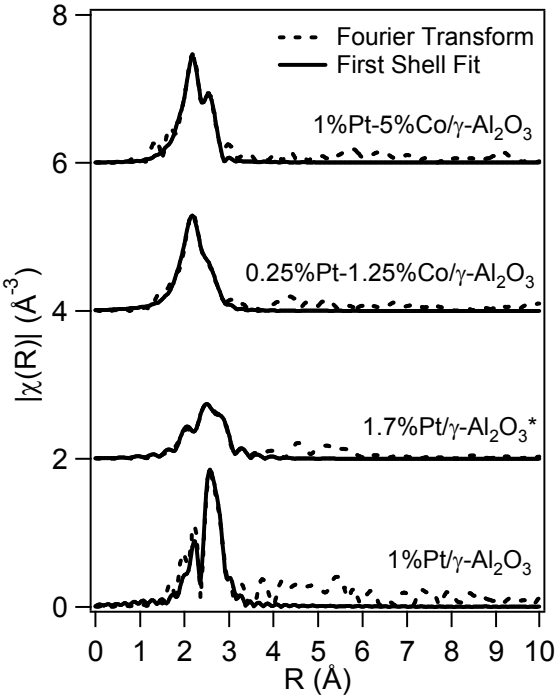

Figure 3.4 Fourier-transformed (magnitude) k^2-weighted EXAFS function (χ(k)) of Pt L_{III}-edge of catalysts after reduction for transformed data and fits.

The parameters that result from fitting the data using Athena and Artemis are located in **Table 3.5**.

Table 3.5 Summary of Pt L_{III}-edge fitting for catalysts. *Indicates data from W.W. Lonergan.[7]

Catalyst	1%Pt/γ-Al_2O_3	1.7%Pt/γ-Al_2O_3*	0.25%Pt-1.25%Co/γ-Al_2O_3	1%Pt-5%Co/γ-Al_2O_3
CN(Pt-Pt)	7.7 ± 0.9	6.2 ± 0.4	3.3 ± 1.5	2.2 ± 1.1
CN(Pt-Co)	--	–	4.4 ± 0.9	4.9 ± 0.9
R(Pt-Pt), Å	2.75 ± 0.01	2.75 ± 0.01	2.71 ± 0.01	2.72 ± 0.01
R(Pt-Co), Å	--	–	2.57 ± 0.01	2.59 ± 0.01
σ^2(Pt-Pt), $Å^2$	0.004 ± 0.001	0.006 ± 0.001	0.007 ± 0.002	0.004 ± 0.001
σ^2(Pt-Co), $Å^2$	--	–	0.009 ± 0.001	0.008 ± 0.001

Analysis of the nearest neighbor coordination numbers (CN) can give information regarding bimetallic bond formation and particle size. The monometallic 1%Pt/γ-Al_2O_3 has a coordination number of 7.7, which is less than the bulk value of 12 assuming a fcc structure. This coordination number is larger than the incipient wetness catalyst coordination number of 6.2, which is expected given the higher particle size of approximately 4 nm compared to approximately 2 nm. The Pt-Pt interatomic distance (R) of 2.75 Å is close to that of bulk Pt-Pt (2.77 Å), which indicates that while Pt nanoparticles are small, the atoms are not overly compressed together. A small (less than or approximately 0.010 $Å^2$) value of the Debye-Waller factor (σ^2), which is a measure of the static and dynamic disorder in a system, indicates that the fit of these parameters with the EXAFS equation is acceptable. With the data for monometallic 1%Pt/γ-Al_2O_3, comparison can be made to draw conclusions about bimetallic Pt-Co catalysts.

It should be noted that data in **Figure 3.4** was initially fit without introducing Co interactions in the first shell and that this fit was unacceptable, as indicated by large Debye-Waller factor σ^2. This is the first indication that bimetallic bonds were formed between Pt and Co atoms. The second indication of the presence of Pt-Co bonds in both 0.25%Pt-1.25%Co/γ-Al_2O_3 and 1%Pt-5%Co/γ-Al_2O_3 is due to the Pt-Co coordination number of 4.4 and 4.9, respectively. The Pt-Pt and Pt-Co coordination numbers are statistically the same for both catalysts, which is expected since the atomic ratio is 1:17 for Pt:Co in both catalysts. This atomic ratio is also the reason for more Pt-Co bonds than Pt-Pt bonds. The third indication of bimetallic bond formation is the intermediate value of interatomic distance (R) for both catalysts. 0.25%Pt-1.25%Co/γ-Al_2O_3 and 1%Pt-5%Co/γ-Al_2O_3 have Pt-Co interatomic distances of 2.57 and 2.59 Å, respectively, which is intermediate between the bulk Co-Co interatomic distance (2.51 Å) and the bulk Pt-Pt interatomic distance (2.77 Å). The fits are acceptable, as indicated by small values of the Debye-Waller factor.

3.5 Motivation for Further Understanding

Although EXAFS results reveal the presence of the Pt-Co bimetallic bonds, the expected enhancement over monometallic parent catalysts was not observed in CO chemisorption or hydrogenation activity. One explanation is that the metal atoms are not rearranging into a Co-subsurface configuration with a Pt monolayer on the surface. Given that metal is reduced chemically, nanoparticles may be thermodynamically stable and may not segregate during high-temperature treatments, which is suggested to produce subsurface configurations and lead to enhanced low-temperature hydrogenation activity.[1, 9] Another explanation of the poor performance is that the excessive solvents used during synthesis may result in excess carbon

adhering to the surface of the nanoparticles, inhibiting reactivity. Another issue regarding this reverse micelle synthesis is the amount of solvents required to produce relatively small quantities of catalyst. To synthesize 1 gram of catalyst, **Table 3.6** shows the amount of water, cyclohexane, Brij-30 and acetone needed.

Table 3.6 Solvents required to synthesize 1 gram of catalyst for monometallic and bimetallic catalysts.

Catalyst	Water (ml)	Cyclohexane (ml)	Brij-30 (ml)	Synthesis volume (ml)	Volume acetone (ml)	Total volume (ml)
0.25%Pt/γ-Al_2O_3	0.1	23.7	0.9	49.5	99.0	148.5
1%Pt/γ-Al_2O_3	0.5	94.8	3.6	198.0	395.9	593.9
0.25%Pt-1.25%Co/γ-Al_2O_3	2.2	416.2	15.9	868.6	1737.2	2605.8
1%Pt-5%Co/γ-Al_2O_3	9.0	1664.6	63.5	3474.3	6948.7	10423.0

Due to the large volumes necessary for the high metal loading bimetallic catalysts, particularly 1%Pt-5%Co/γ-Al_2O_3, smaller batches than 1 gram (0.3-0.5 grams) were synthesized. This is not ideal, given that some techniques (CO pulse chemisorption, EXAFS) require at least 0.1 grams of catalyst for a single run. Using smaller quantities of solvents may result in a cleaner surface and may enhance activity. However, altering the chemistry of reverse micelle synthesis can impact micelle size and uniformity, which will in turn impact particle size and particle size distribution. It is important to investigate how different parameters may affect these variables before choosing new synthesis values. Due to the large parameter space of the system and difficulty in predicting how changing variables may impact particle size and reactivity, a design of experiments was used in order to evaluate these effects.

3.6 Fractional Factorial Design of Experiments

One of the most effective methods to investigate the parameter space of a system is a factorial design of experiments. A full factorial design with k factors will result in 2^k experiments. If one is interested is the effect of some variable *x* on an outcome *y*, a general model can be written as follows:

$$y = \beta_0 + \sum_{i=1}^{k} \beta_i x_i + \sum_{i=1}^{k}\sum_{j=1}^{k} \beta_{ij} x_i x_j + \sum_{i=1}^{k}\sum_{j=1}^{k}\sum_{l=1}^{k} \beta_{ijl} x_i x_j x_l + \ldots + \varepsilon \quad \textbf{(3.1)}$$

In this equation β_0 is the grand average, β_i is the coefficient related to the main effect of factor *i*, β_{ij} is the coefficient related to the two-way interaction effect of the i^{th} and j^{th} factors, β_{ijl} is the coefficient related to the three-way interaction effect of factors *i*, *j*, *l*, et cetera, and ε is unavoidable fluctuation. The question that arises, particularly when dealing with a large parameter space, is whether these higher-order interactions are important. If they are not incredibly important, a fractional factorial design of experiments can be implemented instead. This design eliminates the ability to estimate the (arguably) unimportant higher-order interaction effects in exchange for investigating more parameters with fewer experiments. Instead of 2^k experiments, it is a 2^{k-p} design = (2^{-p}) fraction of the full 2^k design. In the case of four parameters to investigate, a fractional design would require 2^4 (16) experiments. With two repetitions, this results in 32 total experiments. Eliminating the three-way interaction of these parameters results in fewer experiments to perform. A half fractional design of experiments decreases the number of experiments from 2^4 to $2^{4-1} = 2^3 = 8$. With repetitions, this results in 16 total experiments.[10]

There are four parameters of interest in the current reverse micelle synthesis chemistry. A half-fractional design of experiments was used to achieve two goals: determine whether parameters can be adjusted to use less solvent and thus

synthesize larger batches of catalyst without affecting particle size, and determine how these parameters affect particle size and distribution. A summary of the four parameters and their possible effect on nanoparticles is listed in **Table 3.7**.

Table 3.7 Summary of four parameters tested in fractional factorial design of experiments.

Variable		Function	Predicted effect on particle size	Reference
M =	[Metal] in H_2O	Determines volume of H_2O	Variable (depends on R), or no effect	[8, 11]
W =	$[H_2O]/[Brij\text{-}30]$	Determines volume of Brij-30	Small W → Small particles	[12, 13]
R =	$[NaBH_4]/[Pt]$	Determines amount of $NaBH_4$	Large R → Rapid reduction → Uniform, small particles	[11]
B =	mol Brij-30 / L Cyclohexane	Determines amount of cyclohexane	None	----

In order to investigate the effect of different synthesis parameters on supported catalyst particle size and distribution, a half-fractional factorial design of experiments was implemented with these four parameters. Two repetitions were performed for each experiment which resulted in 16 total syntheses necessary. **Table 3.8** lists all required syntheses and their respective values for each parameter. Low and high values were chosen for each parameter.

Table 3.8 Values of parameters for half-fractional factorial design. Color-coding refers to repetitions for each run.

Run #	Order	M	R	W	B
6	R1	0.3	10	3	0.1
3	R2	0.05	20	1	0.5
7	R3	0.05	20	3	0.1
6	R4	0.3	10	3	0.1
8	R5	0.3	20	3	0.5
8	R6	0.3	20	3	0.5
4	R7	0.3	20	1	0.1
5	R8	0.05	10	3	0.5
2	R9	0.3	10	1	0.5
5	R10	0.05	10	3	0.5
1	R11	0.05	10	1	0.1
2	R12	0.3	10	1	0.5
3	R13	0.05	20	1	0.5
4	R14	0.3	20	1	0.1
1	R15	0.05	10	1	0.1
7	R16	0.05	20	3	0.1

0.5 gram samples of 1%Pt/γ-Al_2O_3 were synthesized for each run. Samples were not pre-treated before supporting on TEM grids in order to remove the effect of pre-treatment conditions. Catalysts were supported on TEM grids and imaged using HAADF imaging on JEM-2010F. **Figure 3.5** is a compilation of images and particle size distributions from all 16 catalysts. Some micrographs show promising results of well-dispersed, small, uniform nanoparticles (R4, R5, R6, R11, R12, R13) while others have poor dispersion. Closer inspection of catalysts in **Figure 3.6** reveals that all catalysts have some areas with large clusters and/or sintered particles (particularly R1, R2, R3, R4, R9) and/or areas of very low dispersion (R7, R14, R15, R16).

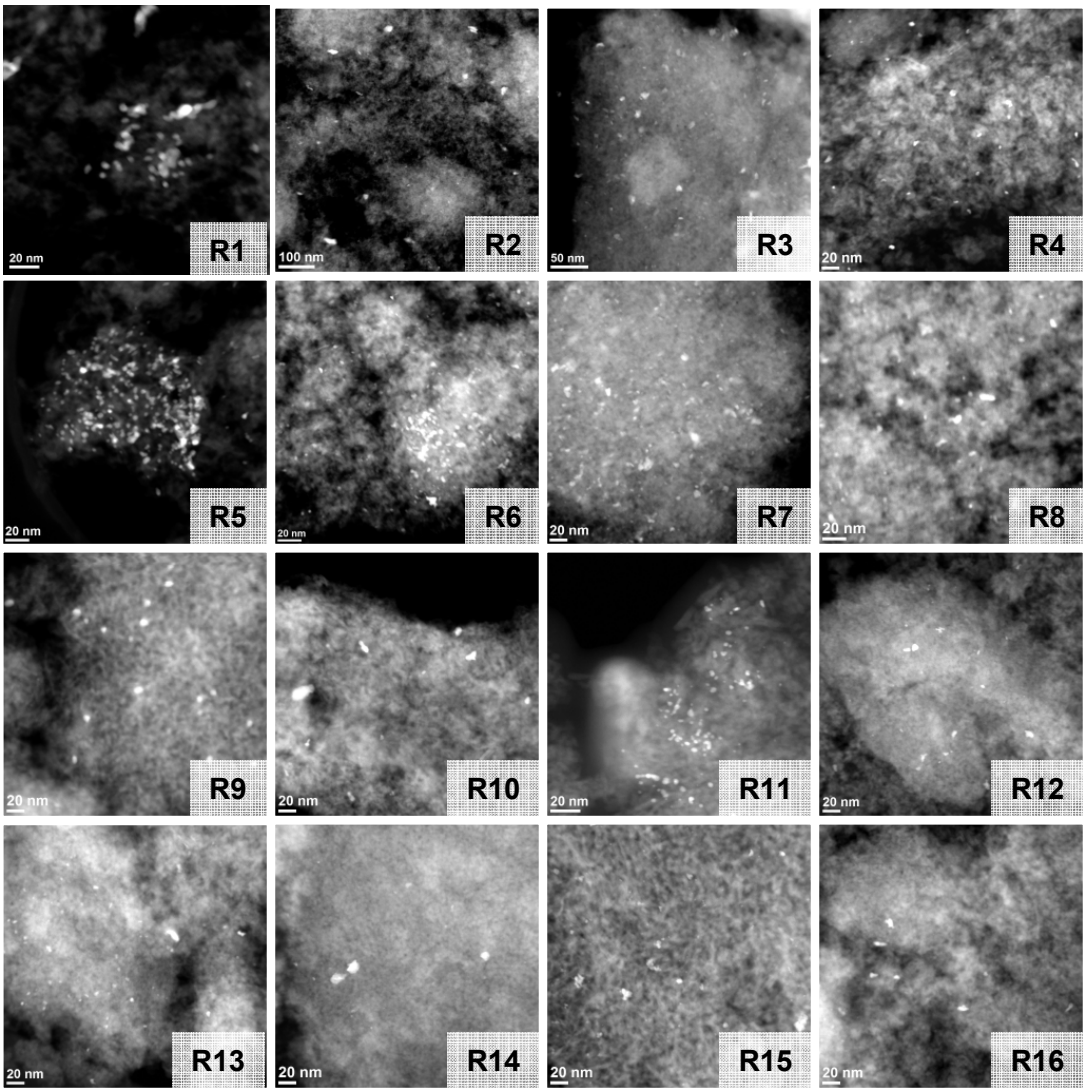

Figure 3.5 **HAADF images of small nanoparticles on catalysts synthesized in the half-fractional design of experiments. Images collected by Ashay Javadekar.**

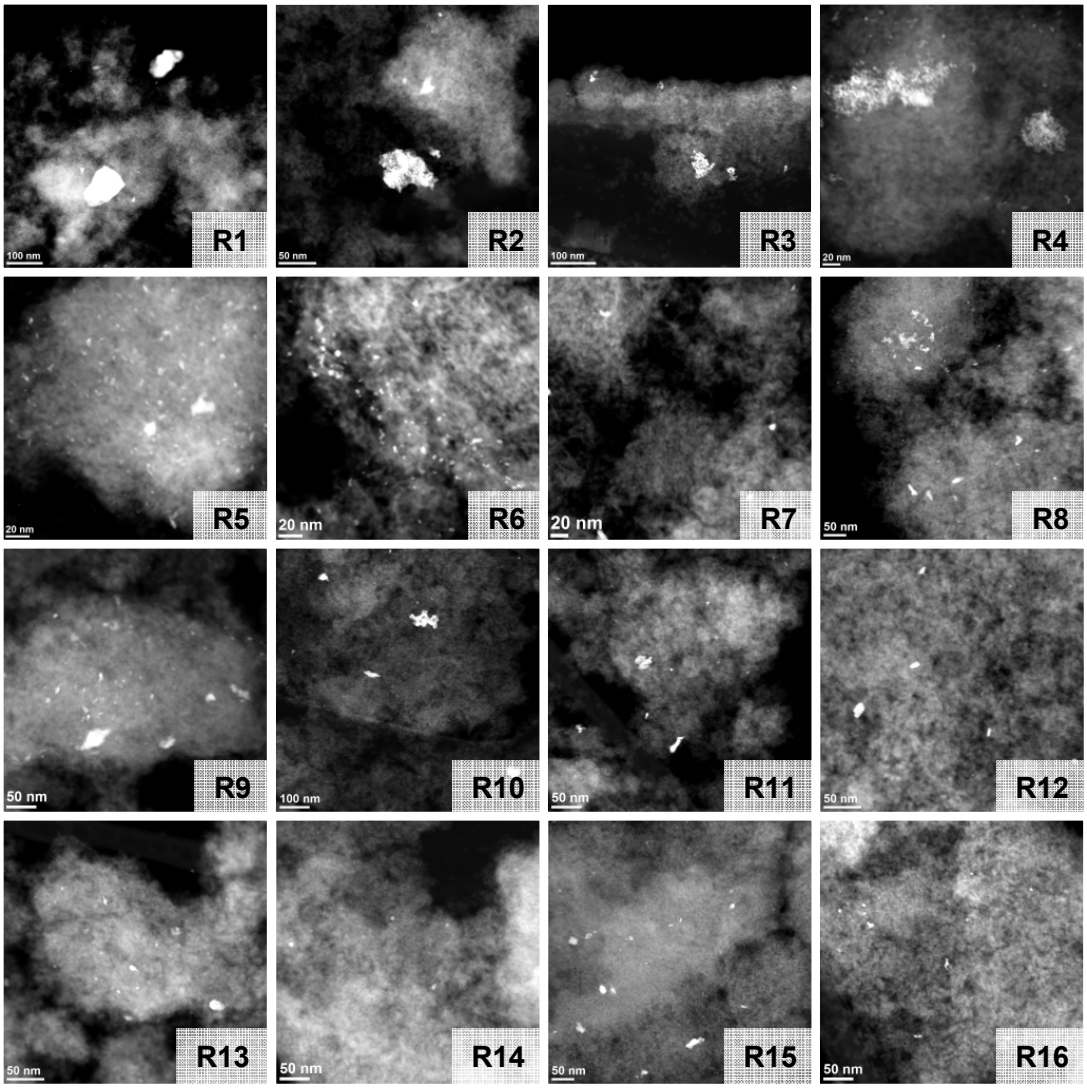

Figure 3.6 HAADF images of agglomerated particles and areas of low-dispersion found in catalysts synthesized in the half-fractional design of experiments. Images collected by Ashay Javadekar.

Particle size and standard deviations were determined for all catalysts and are displayed in **Table 3.9**.

Table 3.9 Particle size statistics of catalysts synthesized in the half-fractional design of experiments. Color codes indicate repetitions.

Run #	Order	M	R	W	B	Average (nm)	Standard deviation (nm)	RSD	Minimum (nm)	Maximum (nm)
6	R1	0.3	10	3	0.1	7.0	3.8	54%	2.9	27.8
3	R2	0.05	20	1	0.5	12.6	7.3	58%	2.6	40.6
7	R3	0.05	20	3	0.1	4.6	2.1	46%	2.0	19.1
6	R4	0.3	10	3	0.1	4.3	1.3	30%	1.7	9.3
8	R5	0.3	20	3	0.5	3.9	1.5	38%	2.0	8.4
8	R6	0.3	20	3	0.5	3.3	1.0	30%	2.0	8.7
4	R7	0.3	20	1	0.1	4.3	1.7	40%	2.0	10.4
5	R8	0.05	10	3	0.5	4.9	1.8	37%	2.6	13.3
2	R9	0.3	10	1	0.5	5.9	2.0	34%	3.1	14.3
5	R10	0.05	10	3	0.5	5.3	1.7	32%	3.1	11.1
1	R11	0.05	10	1	0.1	2.8	0.7	25%	1.6	6.1
2	R12	0.3	10	1	0.5	4.7	1.8	38%	1.7	9.1
3	R13	0.05	20	1	0.5	3.6	0.8	22%	2.3	6.7
4	R14	0.3	20	1	0.1	5.8	2.1	36%	2.9	11.5
1	R15	0.05	10	1	0.1	3.2	1.1	34%	2.0	7.4
7	R16	0.05	20	3	0.1	4.4	1.2	27%	2.2	8.4

Some particle sizes and RSD's are similar between repetitions: R5 (3.9 nm, 38% RSD) and R6 (3.3 nm, 30% RSD), R8 (3.9 nm, 37% RSD) and R10 (5.3 nm, 32% RSD), R11 (2.8 nm, 25% RSD) and R15 (3.2 nm, 34% RSD). However for some repetitions, there is significant variability. Significant variability in particle size and/or RSD is present between repetitions R2 (12.6 nm, 58% RSD) and R13 (3.6 nm, 22% RSD). Similar variations are observed between R1 (7.0 nm, 54% RSD) and R4 (4.3 nm, 30% RSD), R3 (4.6 nm, 46% RSD) and R16 (4.2 nm, 27% RSD), R11 (2.8 nm, 25% RSD)

and R15 (3.2 nm, 34% RSD). Ideally, a narrow distribution is characterized by a deviation around the average of 15-20%, which none of these achieve.

The primary goal of performing a half-fractional factorial design of experiments was to determine whether parameters can be adjusted to use less solvent and thus synthesize larger batches of catalyst without affecting particle size, and determine what parameters do affect particle size. Due to random error in the data it was not possible to determine whether the variables had a statistically significant effect on particle size and standard deviation. Given that most parameter sets averaged around 3-5 nm, one could draw certain conclusions about adjusting synthesis parameters to synthesize larger batches without affecting particle size. However, as shown in **Figure 3.6**, all catalysts had areas of low dispersions and agglomerated particles. While statistical analysis of the data was inconclusive, there is a positive outcome from negative results. Even over a larger range of parameters for this system, random error dominates over the control of this synthesis chemistry and so another synthesis method should be investigated.

3.7 Discussion and Conclusions

Two Pt-Co catalysts of identical atomic ratios (1:17 Pt:Co) but different weight loadings (0.25%Pt/1.25%Co and 1%Pt/5%Co) supported on γ-Al_2O_3 were synthesized by reverse micelle synthesis in an attempt to synthesize uniform nanoparticles. CO pulse chemisorption was used as an indication of active sites and showed that bimetallic catalysts had lower uptakes than the monometallic Pt parent catalyst. HAADF imaging revealed that particles were around 4 nm, which is twice that of the average particle size reported for monometallic 1.7%Pt/γ-Al_2O_3 synthesized using incipient wetness impregnation.[7] By monitoring the peak heights of reactants

and products in a batch system during FTIR spectroscopy the activity of catalysts for benzene hydrogenation was investigated. As expected from low CO uptake during CO pulse chemisorption, bimetallic catalysts were inactive compared to their parent monometallic Pt catalysts. EXAFS confirmed the formation of Pt-Co bimetallic bonds, though the enhanced activity that generally accompanies bimetallic bond formation was not observed.

A half-fractional factorial design of experiments was employed to investigate the effect of parameters on monometallic 1%Pt/γ-Al_2O_3 particle size to determine whether smaller quantities of solvents could be used and thus result in cleaner catalyst sites and larger catalyst batches. Due to the high scatter in particle size and standard deviations within repetitions, statistical analysis could not be performed. All catalysts synthesized had areas of low dispersion and agglomerated particles, regardless of parameter values.

Given the poor performance of bimetallic catalysts and lack of reproducibility observed while varying synthesis parameters, further research with this reverse micelle synthesis recipe was not performed and a different chemistry was investigated.

3.8 References

[1] M.P. Humbert, J.G. Chen, *Journal of Catalysis* **257** (2008) 297.

[2] S. Lu, W.W. Lonergan, J.P. Bosco, S. Wang, Y. Zhu, Y. Xie, J.G. Chen, *Journal of Catalysis* **259** (2008) 260.

[3] J.R. Kitchin, J.K. Nørskov, M.A. Barteau, J.G. Chen, *Journal of Chemical Physics* **120** (2004) 10240.

[4] R. Vijay, C.M. Snively, J. Lauterbach, *Journal of Catalysis* **243** (2006) 368.

[5] R. Vijay, *Doctoral Dissertation* (2007) 232.

[6] A.K. Neyestanaki, P. Mäki-Arvela, H. Backman, H. Karhu, T. Salmi, J. Väyrynen, D.Y. Murzina, *Journal of Catalysis* **218** (2003) 267.

[7] W.W. Lonergan, D.G. Vlachos, J.G. Chen, *Journal of Catalysis* **271** (2010) 239.

[8] X. Zhang, K.-Y. Tsang, K.-Y. Chan, *Journal of Electroanalytical Chemistry* **573** (2004) 1.

[9] N.A. Khan, L.E. Murillo, J.G. Chen, *J. Phys. Chem. B* **108** (2004) 15748.

[10] B.A. Ogunnaike, Random Phenomena: Fundamentals of Probability and Statistics for Engineers. CRC Press, New York, 2010.

[11] D.-H. Chen, S.-H. Wu, *Chemistry of Materials* **12** (2000) 1354.

[12] I. Lisiecki, M.P. Pileni, *Journal of American Chemical Society* **115** (1992) 3887.

[13] Y. Lee, J. Lee, C.J. Bae, J.-G. Park, H.-J. Noh, J.-H. Park, T. Hyeon, *Advanced Functional Materials* **15** (2005) 503.

Chapter 4

SYNTHESIS AND CHARACTERIZATION OF SUPPORTED CATALYSTS CONTAINING PLATINUM AND NICKEL

4.1 Applications of Platinum-Nickel Catalysts

There is a growing interest in supported catalysts containing Pt and Ni due to their enhanced activity and selectivity in many reactions. One promising technology is a polymer-electrolyte membrane (PEM) fuel cell which converts chemical energy into electrical energy. H_2 and O_2 molecules are split on the anode and cathode sides of the fuel cell, respectively. Electrons from the anode side are passed through a circuit, providing electricity, then recombine with O_2 on the cathode side to produce water, a harmless byproduct. One of the limitations with this technology is the oxygen-reduction reaction (ORR) that occurs on the cathode side. The U.S. Department of Energy's Argonne National Laboratory studied the ORR activity of Pt-Ni alloy surfaces under UHV conditions. They found that a Pt-Ni alloy inhibits hydroxide formation on the Pt surface. Hydroxides adsorbed on the surface inhibit the oxygen interaction with surface metal atoms and lowers ORR activity.[1]

Currently, Ni and Pt catalysts are also used in industry for hydrogenation of aromatics. High aromatic content in diesel fuel has been recognized to lower fuel quality in diesel and contributes to the formation of hazardous emissions in gasoline. As a result, the automobile industry has an interest in reducing the aromatic content to improve fuel quality.[2] Research has shown that Pt-Ni bimetallic catalysts convert

benzene to cyclohexane at low temperatures (343 K), which would lead to energy savings in an industrial plant.[3]

Besides application in the transportation sector, Pt-Ni catalysts are useful in manufacturing chemicals and commercial goods. For use in the production of synthetic polymers, benzene hydrogenation is of particular interest. Polyamides (nylons) account for more than 80% of the worldwide synthetic fiber production. Furthermore, cyclohexane, a product of benzene hydrogenation, accounts for 93% of the adipic acid production, an important reactant for the production of Nylon 6 and Nylon 66.[4]

Another environmental concern is the effect of 1,3-butadiene in the isobutene stream produced by steam cracking of naphtha or catalytic cracking of gas oil. Traces of 1,3-butadiene (up to 1%) can poison the dimerization catalysts used in catalytic distillation, which converts isobutene to isooctane. Isooctane is a high-octane rated gasoline component that has the potential to replace methyl tertiary butyl ether (MTBE) gasoline additives which have negative effects on humans and plants.[5] An effective catalyst to hydrogenate 1,3-butadiene is crucial to maintaining an efficient dimerization catalyst. Research has shown that catalysts containing Pt and Ni enhanced 1,3-butadiene hydrogenation activity over their monometallic parent catalysts.[6]

Due to the varied applications of Pt-Ni catalysts, many surface science studies have been conducted with this bimetallic system. Of interest in the current thesis is whether these observations extend to model supported catalyst systems synthesized using a different reverse micelle synthesis chemistry than the one described in Chapter 3. Also of interest is whether these model supported catalysts

have similar activity as those synthesized using industrial catalyst synthesis methods, such as incipient wetness impregnation.

4.2 Catalyst Impregnation Sequences

Catalysts in this study were synthesized using reverse micelle synthesis in order to compare to catalysts synthesized using incipient wetness impregnation. Given the extensive analysis performed on γ-Al_2O_3-supported Pt-Ni bimetallic catalysts, this was chosen as the probe catalyst.[6] An atomic ratio of 1:3 for Pt:Ni was chosen, corresponding to 1.67% by weight Pt and 1.50% by weight Ni. Two impregnation sequences were utilized to determine the effectiveness of reverse micelle synthesis.

4.2.1 Step-Impregnation of Catalysts

Step-impregnated incipient wetness catalysts were previously synthesized and characterized by W.W. Lonergan of the Chen group.[6] Pt and Ni precursor solutions were made by dissolving $Ni(NO_3)_2$-$6H_2O$ (Alfa Aesar) and $Pt(NH_3)_4(NO_3)_2$ (Alfa Aesar) metal precursors separately in enough DI water to fill the pores of γ-Al_2O_3 (Alfa Aesar, 80-120 m^2/g) support (approximate pore volume = 0.6 ml/g support). First, a monometallic Ni was impregnated onto γ-Al_2O_3. This catalyst was dried in air at 373 K for 10 hours and calcined at 563 K for 2 hours. Then the Pt precursor solution was impregnated onto the Ni/γ-Al_2O_3 catalyst. This catalyst was dried in air at 373 K for 10 hours and calcined at 563 K for 2 hours.

To incorporate reserve micelle synthesis, the following procedure was developed, modified from literature.[7] Two solutions were mixed with the following volume percentages: 15% DI water, 10% Triton X-100 surfactant ($C_{14}H_{22}O(C_2H_4O)_n$, n~9.5 on average, Alfa Aesar), 40% 2-propanol co-surfactant (Fisher Scientific), 35%

cyclohexane (Fisher Scientific). One aqueous solution contained 0.04 M $Ni(NO_3)_2$-$6H_2O$ dissolved in DI water. The concentration of N_2H_4 (50% N_2H_4 by volume, Sigma-Aldrich) was 0.3 M. The amount of DI water in the metal salt solution was calculated by maintaining the concentration of metal in water as 0.04 M. The amount of metal salt required was dictated by the desired catalyst mass and desired metal weight percent (1.5 wt% Ni). Since the volume percent of water in the entire metal solution was 15%, the total volume of the entire metal solution could be calculated. Using this total volume, the volumes of Triton X-100, 2-propanol and cyclohexane were calculated. The volume of reductant required in the second solution was calculated by maintaining the concentration of reductant in water as 0.3 M. Since the N_2H_4 reductant used was 50% water by volume, the amount of water used in the reductant solution was equal to that of the metal solution minus half the volume of the N_2H_4. The reductant solution had the same volumes of Triton X-100, 2-propanol and cyclohexane as the metal solution. The ω parameter, $[H_2O]$ / [Triton X-100 + 2-propanol], was 1.0. The values used for producing enough solvents to synthesize 4.00 grams of 1.50 wt% Ni/γ-Al_2O_3 are shown in **Table 4.1**.

Table 4.1 Synthesis parameters used to synthesize 4 grams of 1.50 wt% Ni/γ-Al_2O_3. Gray cells indicate adjustable values.

Defined Parameters	
Parameter	Value
[M] in H_2O (mol/L)	0.04
[N_2H_4] (mol/L)	0.30

Solvent	Volume Fraction
H_2O	15%
Triton X-100	10%
2-propanol	40%
Cyclohexane	35%

Determined by Catalyst	
Parameter	Value
Amount of Catalyst (g)	4.00
Wt % Pt*	1.67%
Wt % Ni	1.50%
*Determines amount of γ-Al_2O_3 needed, not used in metal "M"	
γ-Al_2O_3 (g)	3.87
Omega, ω	1.0

Measured for Catalyst Synthesis		
Component	Beaker 1	Beaker 2
$Ni(NO_3)_2$-$6H_2O$ (g)	0.30	--
Water (ml)	25.56	25.32
Triton X (ml)	17.04	17.04
2-propanol (ml)	106.23	106.23
Cyclohexane (ml)	59.63	59.63
N_2H_4 (ml)	--	0.48
Total volume (ml)	~ 420	
Volume acetone (ml)	~ 840	

To yield 4.00 grams of catalyst, two aqueous solutions were created: one containing 0.30 g of $Ni(NO_3)_2$-$6H_2O$ metal salt and 25.56 ml DI water, the other containing 0.48 ml N_2H_4 and 25.32 ml water. 59.63 ml cyclohexane and 106.24 ml 2-propanol were added to each solution. While under rigorous stirring, 17.04 ml Triton X-100 was added to each solution. Upon addition of the surfactant solutions became transparent, serving as an indication of the formation of micelles. Solutions were stirred separately for one hour to allow micelle size to equilibrate. The reductant

solution was added quickly to the metal solution and the observed change in color (pale green to pink for Ni metal) indicated the reduction reaction. After stirring overnight, 3.87 g of γ-Al_2O_3 support was added to the solution and then the solution was titrated with acetone (twice the volume of the total synthesis solution) to disrupt the micelles and precipitate the nanoparticles onto the support. The supernatant was decanted and the catalyst powder was shaken and rinsed copiously with acetone to remove surfactant from supported particles. Catalysts were cleaned prior to characterization in order to further remove residual surfactant. Cleaning involved ramping to 373 K in O_2 (Keen) over 2 hours, holding for 2 hours at 373 K, followed by a 2 hour ramp to 673 K and a subsequent 2 hour hold.

The synthesis method above yields a 1.53 % by weight Ni/γ-Al_2O_3 catalyst. Depending on the weight of Ni/γ-Al_2O_3 catalyst that was to be impregnated with Pt, the appropriate amount of Pt was added by incipient wetness to yield a 1:3 atomic ratio of Pt:Ni. For example, a 0.5-gram batch of catalyst would require 0.02 grams of $Pt(NH_3)_4(NO_3)_2$ salt dissolved in enough DI water to saturate the pores in γ-Al_2O_3. This solution was added dropwise to the Ni/γ-Al_2O_3. The catalyst was dried in air at 373 K for 10 hours and calcined at 563 K for 2 hours.

4.2.2 Co-Impregnation of Catalysts

Co-impregnation using incipient wetness impregnation involved dissolving both $Ni(NO_3)_2$-$6H_2O$ and $Pt(NH_3)_4(NO_3)_2$ metal precursors in enough DI water to fill the pores of γ-Al_2O_3 support. This catalyst was dried in air at 373 K for 10 hours and calcined at 563 K for 2 hours. This catalyst was synthesized and characterized by W.W. Lonergan.[6]

Co-impregnation using reverse micelle synthesis was performed by dissolving both $Ni(NO_3)_2$-$6H_2O$ and $Pt(NH_3)_4(NO_3)_2$ metal precursors in the aqueous solution. This affects the amount of water in solution and thus all other components. The procedure is the same as that described for Ni in the previous section. A table containing the values used for producing enough solvents to synthesize 1.50 grams of 1.5 wt% Ni, 1.7 wt% Pt supported on γ-Al_2O_3 is shown in **Table 4.2**.

Table 4.2 Synthesis parameters used to synthesize 1.50 grams of 1.67 wt% Pt / 1.50 wt% Ni/γ-Al_2O_3. Gray cells indicate adjustable values.

Defined Parameters	
Parameter	Value
[M] in H_2O (mol/L)	0.04
[N_2H_4] (mol/L)	0.30
Solvent	Volume Fraction
H_2O	15%
Triton X-100	10%
2-propanol	40%
Cyclohexane	35%

Determined by Catalyst	
Parameter	Value
Amount of Catalyst (g)	1.50
Wt % Pt	1.67%
Wt % Ni	1.50%
Both metal % determine amount of γ-Al_2O_3 needed	
γ-Al_2O_3 (g)	1.45
Omega, ω	1.0

Measured for Catalyst Synthesis		
Component	Beaker 1	Beaker 2
$Pt(NH_3)_4(NO_3)_2$	0.05	
$Ni(NO_3)_2$-$6H_2O$ (g)	0.11	--
Water (ml)	12.80	12.68
Triton X (ml)	8.53	8.53
2-propanol (ml)	53.19	53.19
Cyclohexane (ml)	29.86	29.86
N_2H_4 (ml)	--	0.24
Total volume (ml)	~ 210	
Volume acetone (ml)	~ 420	

Nomenclature for step and co-impregnated catalysts synthesized using reverse micelles and incipient wetness impregnation is listed in **Table 4.3.**

Table 4.3 Catalyst nomenclature and synthesis steps.

Step-impregnation

Step	Metal	1Pt-3Ni**(M)**/γ-Al_2O_3	1Pt-3Ni/γ-Al_2O_3
1	1.50 wt% Ni	Reverse micelle **(M)**	Incipient wetness
2	1.67 wt% Pt	Incipient wetness	Incipient wetness

Co-impregnation

Step	Metal	Co-**M** 1Pt3Ni/γ-Al_2O_3	Co-IW 1Pt3Ni/γ-Al_2O_3
1	1.50 wt% Ni 1.67 wt% Pt	Reverse micelle **(M)**	Incipient wetness

4.3 Catalyst Characterization

4.3.1 Analysis of Surface Area Using Pulse CO Chemisorption

Pulse CO chemisorption was performed for all catalysts as an estimation of the number of active sites on the catalyst. For consistency, 10 pulses were included in the analysis for monometallic catalysts and 33 pulses were included in the analysis for bimetallic catalysts.

4.3.1.1 Pulse CO Chemisorption for Step-Impregnated Catalysts

Results from pulse CO chemisorption for step-impregnated catalysts are listed in **Table 4.4**.

Table 4.4 CO uptake and dispersions for monometallic Pt, Ni and step-impregnated Pt-Ni catalysts. *Data from W.W. Lonergan reanalyzed for consistency.[6]

Catalyst	CO uptake (μmol CO / g catalyst)	Dispersion (%)
3Ni**(M)**/γ-Al_2O_3	4.4	1.7
1Pt/γ-Al_2O_3*	28.0	32.7
1Pt-3Ni**(M)**/γ-Al_2O_3	45.1	27.8
1Pt-3Ni/γ-Al_2O_3*	47.0	28.4

The 3Ni**(M)**/γ-Al_2O_3 catalyst has little uptake compared to monometallic 1Pt/γ-Al_2O_3: 4.4 μmol/g compared to 28.0 μmol/g. Low CO uptake could be explained by the formation of NiO or $NiAl_2O_4$ during high-temperature heat treatments in O_2 which are difficult to reduce to metallic Ni.[8] CO uptake and metal dispersion for both micelle and incipient wetness bimetallic catalysts are similar: 45.1 μmol/g catalyst for 1Pt-3Ni**(M)**/γ-Al_2O_3 and 47.0 μmol/g catalyst for 1Pt-3Ni/γ-Al_2O_3. Given that the low uptake for the 3Ni**(M)**/γ-Al_2O_3 compared to its incipient wetness counterpart does not adversely affect the uptake of the bimetallic 1Pt-3Ni**(M)**/γ-Al_2O_3 compared to incipient wetness, most of the CO uptake appears to occur on the monometallic Pt sites and not Ni sites. The extent of active sites on Pt available for CO adsorption are arguably the same amount of sites for both catalysts, given the same synthesis step of incipient wetness of Pt.

4.3.1.2 Pulse CO Chemisorption for Co-Impregnated Catalysts

Results from pulse CO chemisorption for co-impregnated catalysts are listed in **Table 4.5**.

Table 4.5 CO uptake and dispersions for monometallic Pt, Ni and co-impregnated Pt-Ni catalysts. *Data from W.W. Lonergan reanalyzed for consistency.[6]

Catalyst	CO uptake (μmol CO / g catalyst)	Dispersion (%)
3Ni**(M)**/γ-Al_2O_3	4.4	1.7
1Pt/γ-Al_2O_3*	28.0	32.7
Co-**M** 1Pt3Ni/γ-Al_2O_3	5.3	3.3
Co-IW 1Pt3Ni/γ-Al_2O_3*	39.2	24.2

The co-**M** 1Pt3Ni/γ-Al_2O_3 catalyst shows very little CO uptake compared to co-IW 1Pt3Ni/γ-Al_2O_3 (5.3 μmol/g catalyst compared to 39.2 μmol/g catalyst, respectively). By comparison, it has similar uptake as 3Ni**(M)**/γ-Al_2O_3. Particle size analysis may provide insight into why co-impregnation with reverse micelle synthesis results in low CO uptake.

4.3.2 Particle Size Analysis Using TEM

Particle size distributions were created by measuring horizontal particle diameter in several collected TEM images.

4.3.2.1 TEM of Step-Impregnated Catalysts

HAADF TEM images and particle size distributions for catalysts synthesized are shown in **Figure 4.1**. The median and average particle sizes, along with standard deviations and RSD's from particle size distributions are shown in **Table 4.6**.

Table 4.6 Particle size distribution statistics of step-impregnated Pt-Ni catalysts. *Indicates data from W.W. Lonergan.[6]

Catalyst	Median diameter (nm)	Average diameter (nm)	Standard deviation (nm)	RSD
3Ni**(M)**, Unsupported	1.9	2.0	0.3	15%
3Ni**(M)**/γ-Al_2O_3	2.2	2.2	0.5	23%
1Pt-3Ni**(M)**/γ-Al_2O_3	1.6	1.7	0.3	18%
1Pt-3Ni/γ-Al_2O_3*	1.3	1.8	1.5	83%

Figure 4.1 a) shows reduced, unsupported average nanoparticle sizes of 2.0 ± 0.3 nm for 3Ni**(M)**. This catalyst was then supported on γ-Al_2O_3, cleaned in pure O_2 (2 hours at 673 K) to help remove solvents, then reduced (1 hour in 50%H_2/He at 723 K). **Figure 4.1 b)** shows this catalyst, 3Ni**(M)**/γ-Al_2O_3, with an average nanoparticle size of 2.2 ± 0.5 nm. This suggests that reduced nanoparticles remain stable throughout cleaning procedures. This is also a good verification that one can use nanoparticle size in the micelle to correlate with final supported particle size. Furthermore, though it was not performed here, correlation between micelle droplet size and supported nanoparticle size could be done. This is a powerful design parameter, since it presents the possibility to determine final particle size from a combination of oil, water and surfactant and analysis using dynamic light scattering without wasting metal and support material.

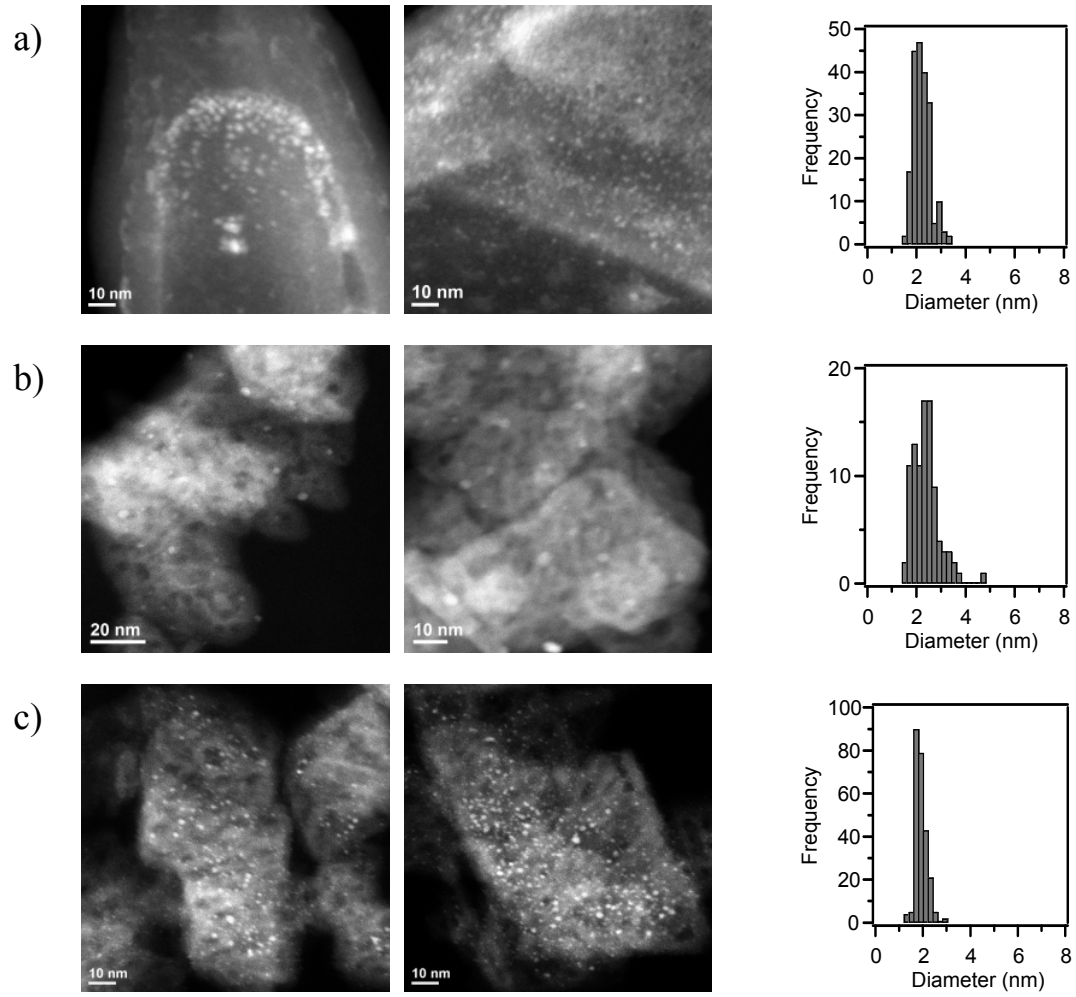

Figure 4.1 HAADF TEM images and particle size distributions of catalysts: a) 3Ni(M), reduced, unsupported nanoparticles, b) 3Ni(M)/γ-Al_2O_3, c) 1Pt-3Ni(M)/γ-Al_2O_3.

Using incipient wetness impregnation, Pt was deposited to the 3Ni**(M)**/γ-Al_2O_3 catalyst after the cleaning procedure described previously. Comparison was made with incipient wetness impregnated catalyst, 1Pt-3Ni/γ-Al_2O_3. Incipient wetness impregnation is capable of producing small nanoparticles (1.8 nm on average), but there are also larger particles present. This results in the presence of particles ranging

from 3-8 nm or even larger.[6] The step-impregnated micelle catalyst 1Pt-3Ni**(M)**/γ-Al_2O_3 also produces small nanoparticles (1.7 nm on average) with a smaller standard deviation of 0.3 nm. This tight distribution is observed in **Figure 4.1 c).** One possible explanation for the smaller deviation is that the metal is reduced chemically, which creates a more stable particle that has less likelihood to sinter and agglomerate during high-temperature pretreatments. Incipient wetness impregnation relies on H_2 treatments to reduce metal oxides into metal nanoparticles. Metal ions are more mobile on the support surface, increasing the likelihood of agglomeration.

The RSD illustrates how each technique affects the average particle size and its distribution. This gives an indication of how narrow a particle size distribution is. Synthesis using incipient wetness results in an RSD of 83%, much higher than the 18% for the catalyst incorporating micelle synthesis. Given that Pt is impregnated by the same method, the benefit of reverse micelle synthesis is hypothetically only seen in counting Ni nanoparticles. It is possible that the high-temperature treatments in O_2 of 3Ni**(M)**/γ-Al_2O_3 could provide a benefit for the impregnation of Pt.

4.3.2.2 TEM of Co-Impregnated Catalysts

HAADF TEM images and particle size distributions for catalysts synthesized using co-impregnation are shown in **Figure 4.2**. The median and average particle sizes, along with standard deviations and RSD's from particle size distributions are shown in **Table 4.7.**

Table 4.7 Particle size distribution statistics of co-impregnated catalysts. *Indicates data from W.W. Lonergan.[6]

Catalyst	Median diameter (nm)	Average diameter (nm)	Standard deviation (nm)	RSD
Co-**M** 1Pt3Ni, Unsupported	1.6	1.6	0.2	13%
Co-**M** 1Pt3Ni/γ-Al_2O_3	2.8	2.9	0.6	21%
Co-IW 1Pt3Ni/γ-Al_2O_3*	1.6	1.9	1.3	68%

Co-impregnation using reverse micelle synthesis produces nanoparticles with an average diameter of 1.6 nm and a narrow distribution of 0.2 nm, shown in **Figure 4.2 a)**. However, upon supporting on γ-Al_2O_3 the average particle size increases to 2.9 nm and the distribution widens slightly to 0.6 nm. By comparison, the monometallic unsupported Ni**(M)** particle diameter is 1.9 nm. This increase in particle diameter to 2.8 nm could be a result of the increase in metal loading during synthesis with 1.67 wt% Pt and 1.50 wt% Ni. The increased metal loading increases the amount of solvents used, which would increase the volume in which reducing agents must reach metal ions, possibly affecting reduction time.

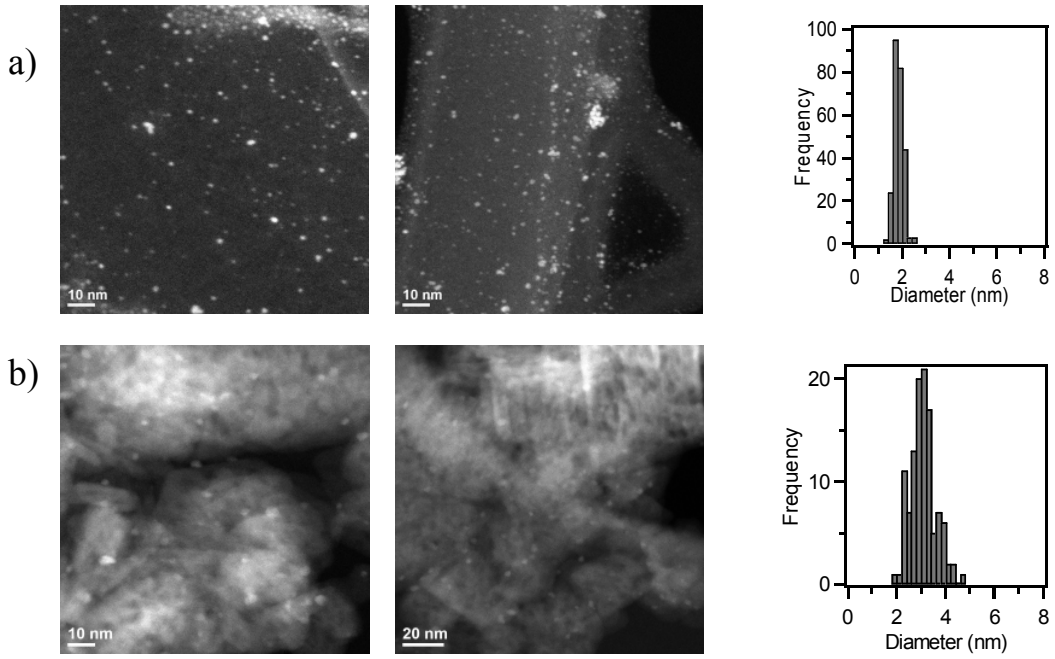

Figure 4.2 TEM images and particle size distributions of co-impregnated catalysts: a) co-M 1Pt3Ni reduced, unsupported nanoparticles, b) co-M 1Pt3Ni/γ-Al_2O_3

Despite the increased particle size, the co-**M** 1Pt3Ni/γ-Al_2O_3 catalyst has a smaller standard deviation of 0.6 nm, compared to co-IW 1Pt3Ni/γ-Al_2O_3 with a standard deviation of 1.3 nm. This suggests that chemical reduction is offering an advantage over high temperature reduction, given the smaller deviation. Given the different average diameters, a smaller RSD will be biased towards the co-**M** catalyst, due to the larger average.

It should be noted that the $Pt(NH_3)_4(NO_3)_2$ precursor was not chemically reduced with N_2H_4 (as would be indicated by a color change to black). Zhang et al. reported that H_2PtCl_6-$6H_2O$ can be chemically reduce with N_2H_4 (a color change to

black was observed). This was also confirmed by laboratory experiments performed by the author. The lack of reduction to metallic Pt may be a reason for the increased particle size. If Pt was adhering to the support in its metal salt phase, the metal particles will be more mobile on the surface during high-temperature treatment and reduction in H_2. This may result in agglomeration, which would decrease the amount of metal available for reaction.

4.3.3 1,3-Butadiene Hydrogenation Activity Analysis Using FTIR Spectroscopy

FTIR spectroscopy was used to evaluate the activity of the catalysts to hydrogenate 1,3-butadiene into 1-butene and n-butane in a batch reactor at 308 K. A carbon balance ensured all products and reactants were accounted for and that no *cis* or *trans* butenes were created during reaction.

4.3.3.1 FTIR Spectroscopy of Step-Impregnated Catalysts

The concentrations of reactant 1,3-butadiene during hydrogenation to products n-butane and 1-butene over step-impregnated catalysts are displayed in **Figure 4.3.** Reactants and products were normalized to 1 by dividing each concentration by the initial concentration of 1,3-butadiene for each catalyst in order to compare to the incipient wetness catalyst. Rate constants are listed in **Table 4.8** and were determined assuming that 1,3-butadiene consumption was first-order**.**

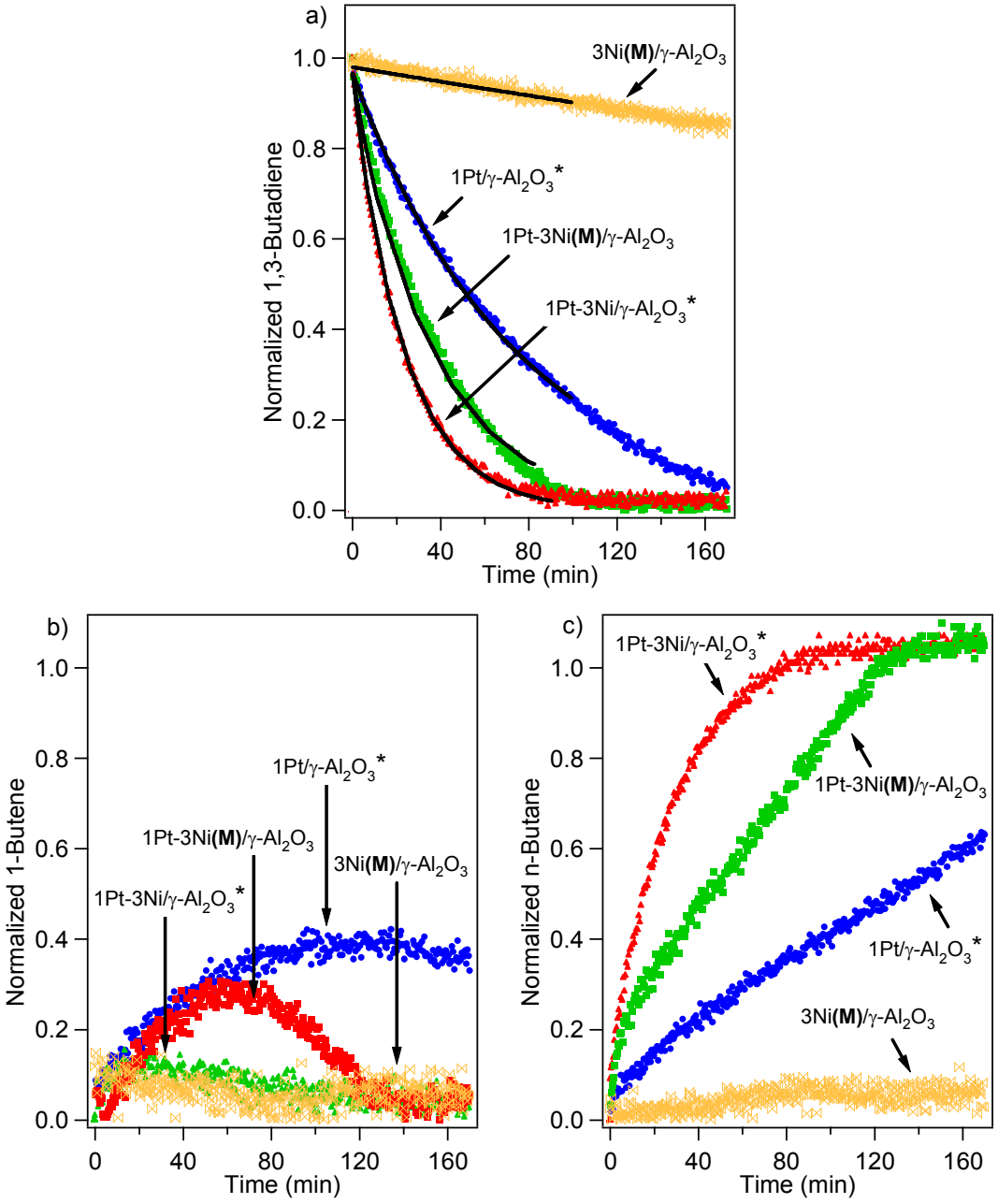

Figure 4.3 **a) 1,3-butadiene consumption, b) 1-butene production, and c) n-butane production during 1,3-butadiene hydrogenation at 308 K over step-impregnated bimetallic and monometallic catalysts. Normalized refers to dividing by initial concentration of 1,3-butadiene. *Indicates data from W.W. Lonergan.[6]**

Table 4.8 First-order consumption rate constants for hydrogenation of 1,3-butadiene over step-impregnated bimetallic and monometallic catalysts. *Indicates data from W.W. Lonergan.[6]

Catalyst	1,3-Butadiene k (min^{-1})	CO uptake (μmol CO / g catalyst)	Dispersion (%)
3Ni**(M)**/γ-Al_2O_3	0.8 x 10^{-3}	4.4	1.7
1Pt/γ-Al_2O_3*	1.4 x 10^{-2}	28.0	32.7
1Pt-3Ni**(M)**/γ-Al_2O_3	3.1 x 10^{-2}	45.1	27.8
1Pt-3Ni/γ-Al_2O_3*	4.8 x 10^{-2}	47.0	28.4

The linear fit for a first-order consumption, displayed as a black line superimposed on the data in **Figure 4.3 a),** shows that the first-order assumption is a valid one. The rate of 1,3-butadiene consumption for 1Pt-3Ni**(M)**/γ-Al_2O_3 is less than 1Pt-3Ni/γ-Al_2O_3, 3.1 x 10^{-2} min^{-1} compared to 4.8 x 10^{-2} min^{-1}; however, 1,3-butadiene was completely consumed by both catalysts by 90 minutes. The differences lie in the products. As shown in **Figure 4.3 b)**, within 60 minutes 1Pt-3Ni**(M)**/γ-Al_2O_3 produces the same amount of 1-butene as monometallic 1Pt/γ-Al_2O_3. After 60 minutes, the 1-butene begins to react to n-butane until the conversion is complete around 120 minutes. However, 1Pt-3Ni/γ-Al_2O_3 produces very little 1-butene and is selective to n-butane. Both catalysts show enhanced activity over monometallic 3Ni**(M)**/γ-Al_2O_3 and 1Pt/γ-Al_2O_3, which have rate constants of 0.80 x 10^{-3} min^{-1} and 1.4 x 10^{-2} min^{-1}, respectively. The reaction did not go to completion on monometallic 1Pt/γ-Al_2O_3. Enhanced activity may be explained by bimetallic Pt-Ni formation, as reported in literature by W.W. Lonergan.[6] EXAFS spectroscopy will determine whether Pt-Ni bimetallic bonds were formed.

4.3.3.2 FTIR Spectroscopy of Co-Impregnated Catalysts

The concentrations of reactant 1,3-butadiene during hydrogenation to produce 1-butene and n-butane over co-impregnated catalysts are displayed in **Figure 4.4.** Reactants and products were normalized to 1 by dividing each concentration by the initial concentration of 1,3-butadiene for each catalyst. Rate constants were determined assuming that 1,3-butadiene consumption was first-order and are listed in **Table 4.9.**

Table 4.9 First-order consumption rate constants for hydrogenation of 1,3-butadiene over co-impregnated bimetallic and monometallic catalysts. *Indicates data from W.W. Lonergan.[6]

Catalyst	1,3-Butadiene k (min^{-1})	CO uptake (μmol CO / g catalyst)	Dispersion (%)
3Ni**(M)**/γ-Al_2O_3	0.8×10^{-3}	4.4	1.7
1Pt/γ-Al_2O_3*	1.4×10^{-2}	28.0	32.7
Co-**M** 1Pt3Ni/γ-Al_2O_3	1.0×10^{-3}	5.3	3.3
Co-IW 1Pt3Ni/γ-Al_2O_3*	9.9×10^{-2}	39.2	24.2

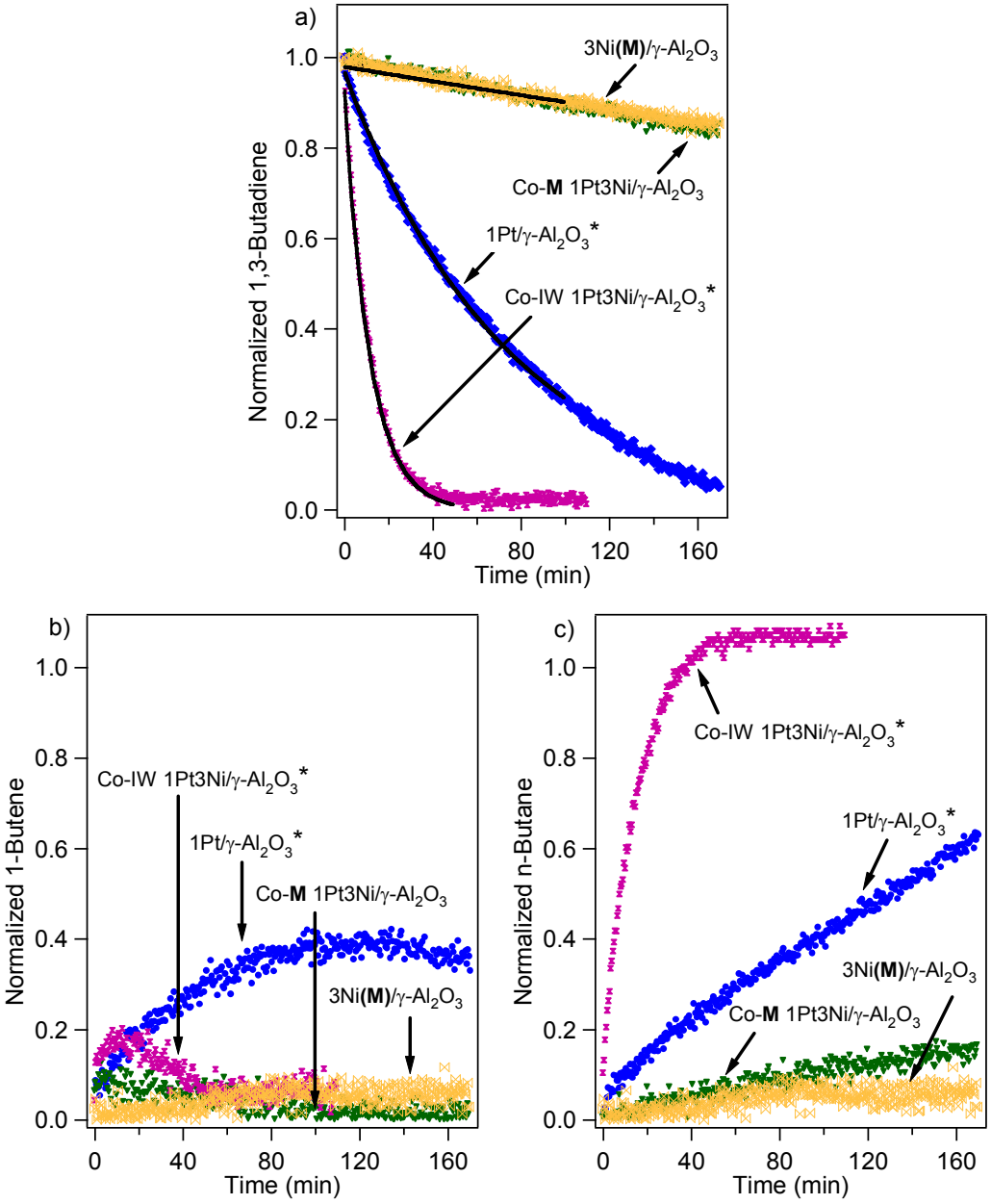

Figure 4.4 **a) 1,3-butadiene consumption, b) 1-butene production, and c) n-butane production during 1,3-butadiene hydrogenation at 308 K over co-impregnated bimetallic and monometallic catalysts. Normalized refers to dividing the concentration with the initial concentration of 1,3-butadiene for each catalyst. *Indicates data from W.W. Lonergan.[6]**

The linear fit for a first-order consumption, shown as a black line superimposed on the data in **Figure 4.4 a),** shows that the first-order assumption is a valid one. The rate of 1,3-butadiene consumption for co-**M** 1Pt3Ni/γ-Al_2O_3 is an order of magnitude less than monometallic 1Pt/γ-Al_2O_3 with a rate constant of 1.0 x 10^{-3} min^{-1} compared to 1.4 x 10^{-2} min^{-1}, respectively, and almost two orders of magnitude less than co-IW 1Pt3Ni/γ-Al_2O_3 with a rate constant of 9.9 x 10^{-2} min^{-1}. The low activity of co-**M** 1Pt3Ni/γ-Al_2O_3 behaves more similarly to monometallic 3Ni**(M)**/γ-Al_2O_3 which has a rate constant of 0.8 x 10^{-3} min^{-1}. EXAFS spectroscopy may provide insight into the extent of bonding between Pt and Ni atoms.

4.3.4 Evaluation of Pt-Ni Bimetallic Bond Formation Using EXAFS Spectroscopy

EXAFS and XANES measurements were performed to elucidate the effect of reduction conditions on oxidation state and investigate the extent of bimetallic interactions between Pt and Ni atoms for step-impregnated and co-impregnated bimetallic catalysts.

4.3.4.1 EXAFS Spectroscopy of Step-Impregnated Catalysts

Figure 4.5 (left) shows the Pt L_{III}-edge XANES of 1Pt-3Ni**(M)**/γ-Al_2O_3 and of Pt foil to serve as a reference for reduced Pt. The spectra shown in **Figure 4.5 (right)** have been treated with background subtraction, edge step normalization and have been k^2-weighted. Because data will be compared with EXAFS data obtained previously for incipient wetness catalysts, the data were Fourier-transformed using a *k*-range between 2 $Å^{-1}$ and 16 $Å^{-1}$. The Hanning window function was used with a sill width of $\Delta k = 2$ $Å^{-1}$.

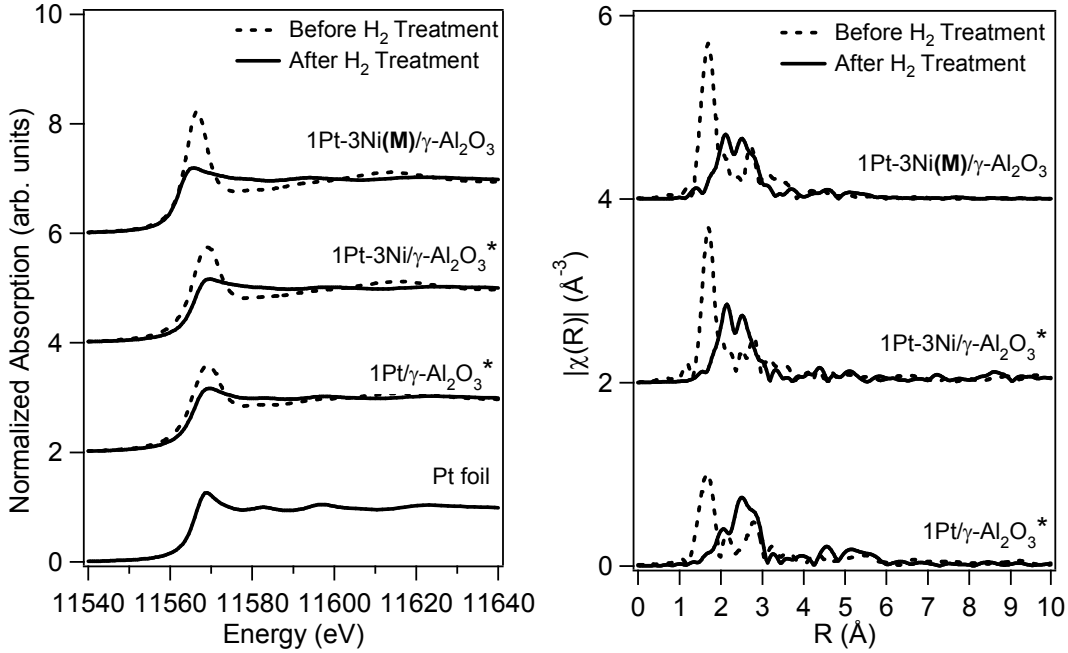

Figure 4.5 Left: Normalized absorption of L_{III}-edge XANES spectrum of monometallic and step-impregnated catalysts before and after reduction. The Pt foil is included to serve as a reference for reduced Pt XANES spectrum. Right: Fourier transformed (magnitude) k^2-weighted EXAFS function (χ(k)) of Pt L_{III}-edge of monometallic and step-impregnated catalysts before and after reduction.*Indicates data from W.W. Lonergan.[6]

The large peaks observed at low R-space for 1Pt-3Ni**(M)**/γ-Al_2O_3 in **Figure 4.5 (right)** are due to Pt-O bond interactions. These peaks are also apparent in monometallic and bimetallic incipient wetness catalysts. After reduction in H_2 these peaks disappear. The resulting peaks at larger values of R are due to Pt-Pt and Pt-Ni bond interactions. These trends are observed in **Figure 4.5 (left)**, where the white line intensity from the catalysts before reduction decreases to resemble that of a Pt foil, indicating that Pt is reduced.

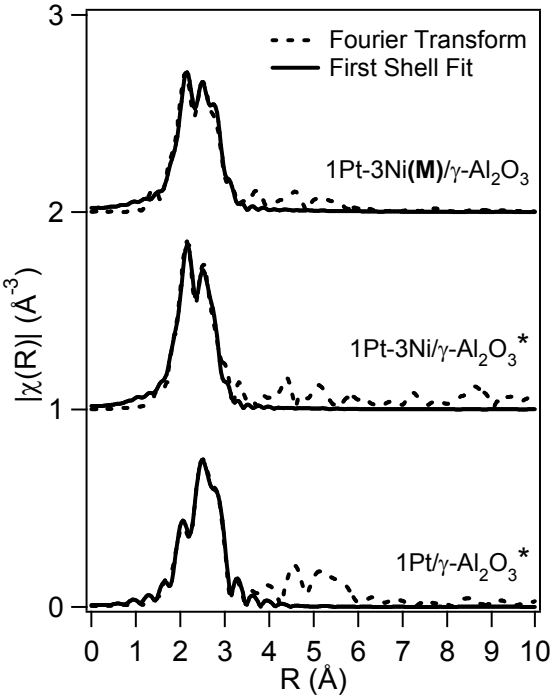

Figure 4.6 Fourier-transformed (magnitude) k^2-weighted EXAFS function ($\chi(k)$) of Pt L_{III}-edge of monometallic and step-impregnated bimetallic catalysts after reduction for transformed data and fits. *Indicates data from W.W. Lonergan.[6]

Figure 4.6 represents the Fourier-transformed experimental data after reduction and the fits obtained used FEFF6 theory. The EXAFS data were fit by incorporating Pt-Pt and Pt-Ni interactions. Given that the Pt-O peaks in **Figure 4.5 (right)** disappear after reduction in H_2, Pt-O contributions were not included in the model. A summary of these values is shown in **Table 4.10**.

Table 4.10 Summary of Pt L_{III}-edge fitting for monometallic and bimetallic step-impregnated catalysts. *Indicates data from W.W. Lonergan.[6]

Catalyst	1Pt/γ-Al_2O_3*	1Pt-3Ni/γ-Al_2O_3*	1Pt-3Ni**(M)**/γ-Al_2O_3
CN(Pt-Pt)	6.2 ± 0.4	4.4 ± 0.7	6.5 ± 0.6
CN(Pt-Ni)	--	2.6 ± 0.6	1.6 ± 0.5
R(Pt-Pt), Å	2.75 ± 0.01	2.72 ± 0.01	2.73 ± 0.01
R(Pt-Ni), Å	--	2.57 ± 0.01	2.56 ± 0.01
σ^2(Pt-Pt), $Å^2$	0.006 ± 0.001	0.007 ± 0.001	0.008 ± 0.001
σ^2(Pt-Ni), $Å^2$	--	0.010 ± 0.002	0.011 ± 0.002

The Debye-Waller parameter, σ^2, is an indication of the disorder in the neighbor distances. Values less than or approximately equal to 0.010 are acceptable; therefore the values listed in **Table 4.10** are acceptable. Analysis of coordination numbers gives information regarding the extent of bimetallic bond formation and particle size. It should be noted that data in **Figure 4.6** was first fit without introducing Ni interactions in the first shell and that this fit was unacceptable. After introducing Ni into the first shell, an acceptable fit was obtained. There are Pt-Ni bonds present in 1Pt-3Ni**(M)**/γ-Al_2O_3, as apparent in a Pt-Ni coordination number of 1.6 ± 0.5. This is lower than the Pt-Ni coordination number of the incipient wetness catalyst 1Pt-3Ni/γ-Al_2O_3, meaning there are fewer Ni atoms surrounding a Pt atom and more Pt atoms surrounding Pt. This is apparent in the larger Pt-Pt coordination number for 1Pt-3Ni**(M)**/γ-Al_2O_3 (6.5 ± 0.6) compared to 1Pt-3Ni/γ-Al_2O_3 (4.4 ± 0.7).

The sum of the coordination numbers for 1Pt-3Ni/γ-Al_2O_3 and 1Pt-3Ni**(M)**/γ-Al_2O_3 is 7.0 ± 0.9 and 8.1 ± 0.8, respectively. Assuming a hemispheric cuboctohedral geometry, Frenkel et al. have predicted particle sizes based on average first shell coordination number. The corresponding particle size ranges from 1.2 to 1.7

nm for 1Pt-3Ni/γ-Al_2O_3 and 1.5 to 2.6 nm for 1Pt-3Ni**(M)**/γ-Al_2O_3. Average particle sizes determined from TEM of 1.8 nm and 1.7 nm, respectively, fall within these ranges.

The Pt-Pt interatomic distances for both Pt-Ni catalysts are around 2.73 Å. This is 0.04 Å less than the bulk metallic Pt-Pt distance of 2.77 Å, which is expected given 2 nm nanoparticles. One would expect that if Pt were bonded to Ni, an intermediate distance between a Pt-Pt bond and Ni-Ni bond would result. Pt-Ni interatomic distances are 2.56 Å, which is 0.7 Å greater than the metallic Ni-Ni interatomic distance (2.49 Å), and 0.21 Å less than the metallic Pt-Pt distance. Both coordination number and interatomic distance results confirm that the Pt-Ni bimetallic bonds have been formed.

4.3.4.2 EXAFS Spectroscopy of Co-Impregnated Catalysts

A customary practice before collecting EXAFS data is to make an initial scan to determine the edge jump of the catalyst. The edge jump is defined as the difference between the absorption before and after the edge, where most X-ray absorption occurs, as illustrated in **Figure 4.7**.

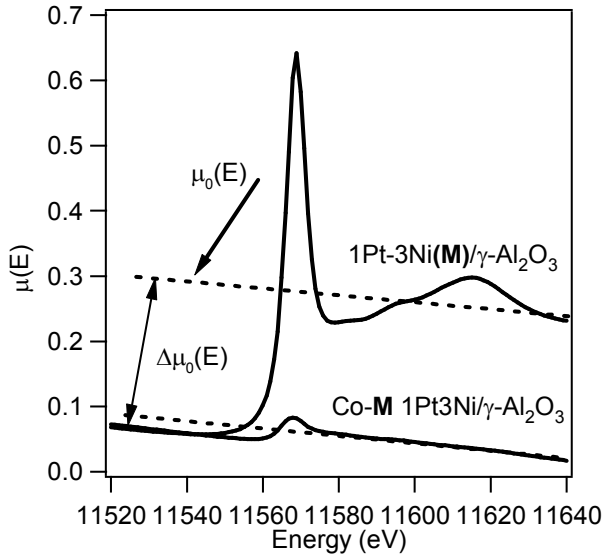

Figure 4.7 X-ray absorption coefficient before and after the Pt L_{III}-edge of step-impregnated and co-impregnated Pt-Ni catalysts.

For a sample of uniform thickness, *t*, the absorption, μ(E), is measured by the ratio of X-ray intensity transmitted through the sample (*I*) to the X-ray intensity sent to the sample (I_0), described in **Equation 4.1**.

$$\mu(E)t = -\ln\left(\frac{I}{I_0}\right) \tag{4.1}$$

The value used to normalize the data used for EXAFS analysis, as shown in **Equation 4.2**, is $\Delta\mu_0$, the measured jump in absorption $\mu(E)$ at absorption edge energy E_0.

$$\chi(E) = \frac{\mu(E) - \mu_o(E)}{\Delta\mu_o(E)} \tag{4.2}$$

A minimum value for acceptable resolution of data is $\Delta\mu_o(E) = 0.1$. As shown in **Figure 4.7** for 1Pt-3Ni**(M)**/γ-Al_2O_3, $\Delta\mu_o(E) = 0.3$. However, for co-**M**

1Pt3Ni/γ-Al_2O_3, $\Delta\mu_o(E)$ = 0.02. This small value indicates X-ray absorption was too low to result in a large enough change in transmitted intensity. One explanation for the small edge jump is that few Pt atoms were on the catalyst, which could also provide explanation for low CO uptake and hydrogenation activity. Further characterization was performed to elucidate the reason behind this low absorption.

4.3.5 Extent of Metal Uptake on Bimetallic Catalysts Using AAS

The extent of metal uptake was analyzed using atomic absorption spectroscopy. In order to do a comparison of metal loading for catalysts synthesized with reverse micelle synthesis, Pt and Ni metal loadings were divided by the metal loading found for co-IW 1Pt3Ni/γ-Al_2O_3. Ideally, 1Pt-3Ni**(M)**/γ-Al_2O_3 would be divided by its incipient wetness counterpart 1Pt-3Ni/γ-Al_2O_3; however, due to limited sample this was not performed. It is assumed that the amount of Pt present in both co-IW 1Pt3Ni/γ-Al_2O_3 and 1Pt-3Ni/γ-Al_2O_3 is the same given that precursors are added to support with the same method. Literature shows that the metal loadings used to determine the amount of metal precursor to dissolve in water for incipient wetness impregnation accurately describe the metal loadings after adsorption onto γ-Al_2O_3, for example: Pt[9, 10], Ni[11], Co[10], and Ba[10].

The absorbance resulting from the dissolved metal of 1Pt-3Ni**(M)**/γ-Al_2O_3 and co-**M** 1Pt3Ni/γ-Al_2O_3 were divided by the absorbance of co-IW 1Pt3Ni/γ-Al_2O_3. Their results are listed in **Table 4.11**. The Ni content for both catalysts synthesized using reverse micelle synthesis is within 15% of the expected Ni content of incipient wetness impregnation. The effect of lower Ni content is observed when fitting EXAFS data; the coordination number for Pt atoms bonded to Ni atoms is smaller for the micelle catalyst 1Pt-3Ni**(M)**/γ-Al_2O_3 than incipient wetness catalyst 1Pt-3Ni/γ-

Al_2O_3 (1.6 ± 0.5 compared to 2.6 ± 0.5). The Pt content for the step-impregnated 1Pt-3Ni**(M)**/γ-Al_2O_3 is within 12% of the expected Pt content from incipient wetness impregnation. However, the Pt content for the co-impregnated co-**M** 1Pt3Ni/γ-Al_2O_3 is 25% of the expected Pt content. This low adsorption of Pt on γ-Al_2O_3 of Pt could be the explanation for low CO uptake, low hydrogenation activity and the reason for low X-ray absorption during EXAFS.

Table 4.11 Relative absorbance of Pt and Ni metals from atomic absorption spectroscopy for step-impregnated and co-impregnated bimetallic catalysts. Absorbance is normalized to co-IW 1Pt3Ni/γ-Al_2O_3.

Catalyst	Ni Content	Pt Content
1Pt-3Ni**(M)**/γ-Al_2O_3	85% ± 1%	88% ± 4%
Co-**M** 1Pt3Ni/γ-Al_2O_3	89% ± 1%	24% ± 1%
Co-IW 1Pt3Ni/γ-Al_2O_3	100% ± 1%	100% ± 5%

4.4 Discussion

One limitation that has been directly observed with reverse micelle synthesis is the difficulty in adsorbing the metal onto the support. After chemical reduction, support is mixed into the micelle solution containing reduced metal particles suspended in surfactant-stabilized water droplets. Acetone was added to destabilize surfactant molecules and allow the metal nanoparticles to adhere to the support. Unfortunately it is difficult to know whether sufficient adsorption of all metal onto the support occurs during this step.

In order to achieve highly-dispersed metallic catalysts, understanding how metal complexes adsorb to oxide surfaces is crucial. J.P. Brunelle in 1978 investigated

fundamental reasons behind why certain metallic complexes adsorb to oxide supports and what governs this adsorption. He focused on the simple principle of surface polarization of an oxide as a function of pH and adsorption of complex ions by electrostatic attraction. Most oxide supports, such as γ-Al_2O_3, are amphoteric and can react either as an acid or base depending on the pH of the solution surrounding the support. In an acid medium, the support surface is positively charged, which results in a layer of negatively-charged ions near this particle. In a basic medium, the support surface is negatively charged with a layer of positively-charged ions around the particle. Between these two cases there exists a pH value where the support surface is not charged. This value corresponds to the point of zero charge (PZC) or isoelectric point of the oxide support.[12] A schematic representation is shown in **Figure 4.8.**

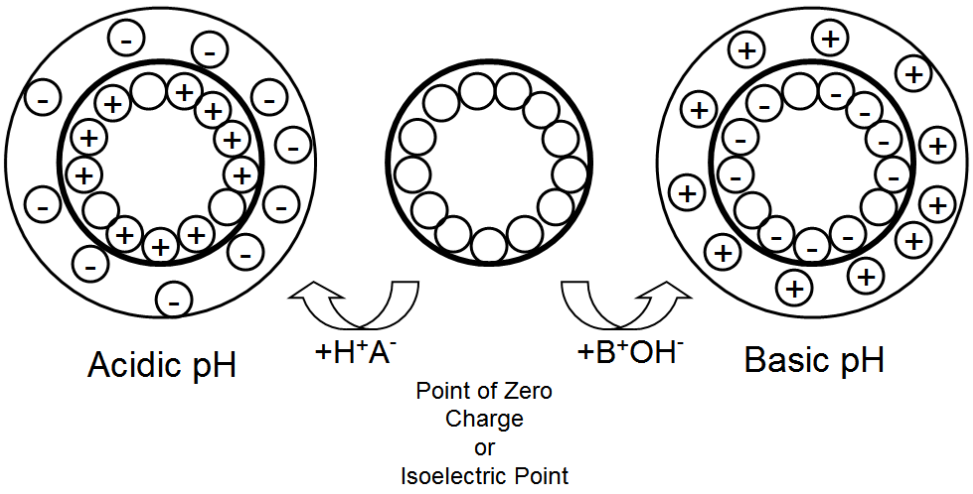

Figure 4.8 Schematic representation of the surface polarization of an oxide particle as a function of solution pH.

An exploratory study regarding the pH throughout reverse micelle synthesis was performed to determine whether a reason for the low adsorption of Pt could be found. As mentioned previously, Pt was not chemically reduced with N_2H_4, as would have been apparent by a color change to black, and therefore one could assume that the precursor was still in its cationic complex form of $Pt(NH_3)_4^{2+}$. According to the previous discussion, good adhesion of Pt would result if the pH of the micelle solution before adding γ-Al_2O_3 was higher than 8.5, the PZC of γ-Al_2O_3.[12] Using a calibrated pH meter (Checker by Hanna) the pH of micelle solutions was monitored throughout the synthesis for the co-impregnated catalyst synthesized with precursors $Pt(NH_3)_4(NO_3)_2$ and $Ni(NO_3)_2$-$6H_2O$. The pH of the precursors dissolved only in DI water was 3.7. After addition of cyclohexane, 2-propanol and Triton X-100 the pH increased to 4.9. The pH of the N_2H_4 dissolved only in DI water was 10.2. After addition of cyclohexane, 2-propanol and Triton X-100 the pH decrease slightly to 9.7. Upon mixing these solutions, the resulting pH was 8.7. This pH is very close to the PZC of γ-Al_2O_3 and is not an ideal condition for adhesion onto the support. It should be noted that this pH of 8.7 is more indicative of a bulk pH and not pH of aqueous solution within micelles, which is the phase in which adsorption of metal onto support occurs. However, a pH of 8.7 in bulk solution may have a greater impact on the resulting surface charge of the support, given that the aqueous solution is a small fraction of the overall solutions. This may affect adsorption of precursor complexes. This may be an explanation for why little Pt adhered in co-impregnation. Furthermore, after the micelles were broken with acetone, the pH decreased to 3.5, well below the PZC and below the range of adhesion

for a cationic complex. With a positively-charged surface due to the acidity, the positive Pt complex has no driving force to adhere to the surface.

The pH has more effect on reverse micelle synthesis than just supporting the metals. Literature suggests that the reducing agent, N_2H_4, is affected by pH of solution and temperature. One example is the effect of reducing agent on the reduction of Ni^{2+} to metallic Ni. Previous research suggests that this reduction occurs in two steps with an intermediate formed with N_2H_4.[13]

$$2Ni^{2+} + 6N_2H_4 \leftrightarrow 2[Ni(N_2H_4)_3]^{2+} \quad \textbf{(4.3)}$$

$$2[Ni(N_2H_4)_3]^{2+} + 4OH^- \leftrightarrow 2Ni + N_2 + 4H_2O + 5N_2H_4 \quad \textbf{(4.4)}$$

The sum of these two steps results in the following equation, which has also been reported elsewhere as the reduction reaction of Ni^{2+} in N_2H_4.[13, 14]

$$2Ni^{2+} + N_2H_4 + 4OH^- \rightarrow 2Ni + N_2 + 4H_2O \quad \textbf{(4.5)}$$

J.W. Park et al. observed a pink solution while reducing $NiCl_2$-$6H_2O$ with N_2H_4at 333 K; however, addition of NaOH to maintain alkalinity resulted in a black solution within 15 minutes, indicating the formation of metallic Ni. They explained their pink solution as a function of molar ratio of N_2H_4/Ni^{2+} and the resulting Ni- N_2H_4-chloride complexes formed.[15] Y.D. Li et al. also observed a pink color when mixing N_2H_4 with their Ni precursor $NiSO_4$-$7H_2O$ at pH lower than 9.5. Their explanation was the formation of $NiSO_4$-$3N_2H_4$. When the pH was adjusted between 9.5 and 10.0 and the temperature was between 358 and 368 K, a black powder formed after reacting for 4 hours.[13] In another paper regarding the synthesis of Ni nanoparticles in water-in-oil microemulsions, D.H. Chen et al. adjusted the pH of their solution to 13 with ammonia solution, which resulted in complete reduction of Ni ions within 1 hour at 343 K. N_2 gas was produced continuously during reaction: another indication of full

reduction. XRD confirmed that only Ni nanoparticles were obtained; no peaks that would indicate NiO, Ni_2O_3, $Ni(OH)_2$ were observed.[14] The reason behind the adjustment of pH to 13 is not provided; however, given the previous discussion of the effect of pH on reduction of Ni^{2+} to metallic Ni with N_2H_4, one could argue that pH adjustment to a basic solution is important in the reduction reaction.

For the synthesis described in this work the pH of the step-impregnation and co-impregnation reverse micelle solution containing only 0.3 M N_2H_4 in water was 10.5 and 10.2, respectively. When mixed with the solution containing only Ni precursor for step-impregnation solution and Pt and Ni precursors for co-impregnation solutions, the pH adjusted to 8.3 and 8.7, respectively. A pink solution formed in both cases. Full reduction of both metals should have turned the solution black. The reasoning behind the formation of a pink precipitate above did not have the same components in common (J.W. Park's explanation involved chlorinated complexes,[15] Y.D. Li's explanation involved sulfur and carbonate-containing complexes[13]) and neither of these components are in the synthesis described here. The hypothesis is that N_2H_4 requires a more basic solution to work effectively as a reducing agent, as demonstrated by the reduction observed after adjusting pH to 13 in D.H. Chen's work.[14] Further investigation with the parameter space regarding N_2H_4 concentration, N_2H_4/Ni molar ratio, and pH is suggested.

4.5 Conclusions

It has been demonstrated that reverse micelle synthesis is capable of synthesizing small, stable nanoparticles supported on γ-Al_2O_3. Two synthesis methods were tested, modeled after previously performed catalyst synthesis using incipient wetness impregnation: step-impregnation, where Ni is synthesized using reverse

micelles and then supported on γ-Al_2O_3, followed by deposition of Pt using incipient wetness impregnation, and co-impregnation, where both Ni and Pt are simultaneously synthesized using reverse micelles and then supported on γ-Al_2O_3. It was found that all catalysts contained small nanoparticles on the order of 2-3 nm. Reverse micelle catalysts showed smaller standard deviations than their incipient wetness counterparts, likely as a result chemical reduction within micelles that stabilized particles and reduced sintering and agglomeration during high-temperature treatments.

The difference in catalyst preparation was apparent in hydrogenation activity and EXAFS data. Step-impregnated catalysts, from reverse micelle and incipient wetness impregnation, performed very similarly for 1,3-butadiene hydrogenation, which was also reflected in their similar CO uptake. After 80 minutes both catalysts consumed all 1,3-butadiene. EXAFS analysis confirmed the presence of bimetallic Pt-Ni bonds, which explains enhanced activity. AAS revealed that Ni and Pt content of the step-impregnated reverse micelle catalyst were within 15% of the incipient wetness catalyst Pt and Ni content.

Co-impregnation catalysts from reverse micelle synthesis behaved similarly to monometallic Ni in 1,3-butadiene hydrogenation and was mainly inactive. The lack of difference in intensity between incident and transmitted X-rays resulted in no EXAFS data collection. From CO chemisorption, hydrogenation activity and EXAFS analysis it was apparent that no bimetallic interaction between Pt and Ni was present. AAS revealed that while Ni content was comparable to co-impregnated incipient wetness catalyst (and the same as Ni content from step-impregnated reverse micelle catalyst), very little Pt was actually adsorbed by the support. This explains the

low activity, low CO uptake and the lack of sufficient X-ray absorption during EXAFS data collection.

Due to the exploratory analysis performed regarding pH of adsorbing solutions, the next step would be to investigate the effect of controlling pH during reverse micelle synthesis. Ideally, as mentioned previously, the metal should be reduced from its ionic complex to a metallic oxidation state of zero, and therefore the pH of adsorbing solution may not greatly impact metal adhesion. However, given that the reducing agent is affected by pH, a study involving the effect of pH on reduction and adsorption is recommended.

4.6 References

[1] L. Yarris, A Boost for Hydrogen Fuel Cell Research. http://newscenter.lbl.gov/news-releases/2007/01/25/a-boost-for-hydrogen-fuel-cell-research/, 2007.

[2] A. Stanislaus, B.H. Cooper, *Catalysis Reviews Science and Engineering* **36** (1994) 75.

[3] S. Lu, W.W. Lonergan, J.P. Bosco, S. Wang, Y. Zhu, Y. Xie, J.G. Chen, *Journal of Catalysis* **259** (2008) 260.

[4] G. Bellussi, C. Perego, *Cattech* **4** (2000) 4.

[5] D. Seth, A. Sarkar, F.T.T. Ng, G.L. Rempel, *Chemical Engineering Science* **62** (2007) 4544.

[6] W.W. Lonergan, D.G. Vlachos, J.G. Chen, *Journal of Catalysis* **271** (2010) 239.

[7] X. Zhang, K.-Y. Tsang, K.-Y. Chan, *Journal of Electroanalytical Chemistry* **573** (2004) 1.

[8] C. Li, Y.-W. Chen, *Thermochimica Acta* **256** (1995) 457.

[9] J.W. Shabaker, R.R. Davda, G.W. Huber, R.D. Cortright, J.A. Dumesic, *Journal of Catalysis* **215** (2003) 344.

[10] R. Vijay, C.M. Snively, J. Lauterbach, *Journal of Catalysis* **243** (2006) 368.

[11] C. Li, Y.-W. Chen, *Thermochimica Acta* **256** (1995) 457.

[12] J.P. Brunelle, *Pure and Applied Chemistry* **50** (1978) 1211.

[13] Y.D. Li, C.W. Li, H.R. Wang, L.Q. Li, Y.T. Qian, *Materials Chemistry and Physics* **59** (1999).

[14] D.-H. Chen, S.-H. Wu, *Chemistry of Materials* **12** (2000) 1354.

[15] J.W. Park, E.H. Chae, S.H. Kim, J.H. Lee, J.W. Kim, S.M. Yoon, J.-Y. Choi, *Materials Chemistry and Physics* **97** (2006) 371.

Chapter 5

FUTURE WORK RECOMMENDATIONS

The main focus of this thesis was to discuss the synthesis of nanoparticles with uniform particle size and narrow distribution. The method that was employed to achieve this goal was reverse micelle synthesis. This technique involves chemically reducing metal precursors in droplets of water stabilized by surfactants (and optionally co-surfactants) dispersed in an oil phase. In general this synthesis technique resulted in uniformly-sized, reduced, unsupported nanoparticles. However, there was difficulty when supporting the nanoparticles onto a high surface area oxide support. A major challenge discussed in Chapter 3 was an issue with low dispersion and agglomeration, even over a wide range of synthesis parameter values before catalysts were cleaned in high temperatures. While the synthesis procedure in Chapter 4 seemed more promising due to uniform particle size and narrow distributions, co-impregnation with high metal loadings resulted in low metal uptake during supporting, possibly due to the pH of micelle solution and its effect on the reducing agent and support surface charge. Given the encouraging results from a step-impregnation synthesis performed with catalysts described in Chapter 4, further discussion for improving this synthesis is provided.

5.1 Effect of pH on Micelle Solutions

As discussed in Chapter 4, the pH of a solution may affect the surface species on γ-Al_2O_3 and thus the preference of adsorption for different cationic or

anionic precursors. Given that reverse micelle synthesis should chemically reduce metal precursors from their ionic salt compounds, the pH of solution should not be of great concern with regards to the effect on metal salt adsorption. However, the metal Pt precursor did not reduce to metallic Pt, as indicated by a lack of color change to black. For the cationic precursor used, a pH solution higher than around 8.5 is preferred so that the surface groups on the oxide support are negatively charged, thus attracting the positively charged precursor ions $Pt(NH_3)_4^{2+}$.[1, 2] The pH of the micelle solution containing the cationic species was 8.7, which is close to the point of zero charge of γ-Al_2O_3. This provides no driving force for adsorption of $Pt(NH_3)_4^{2+}$, which was the explanation for low Pt adsorption for co-micelle impregnated catalysts.

Literature suggests that extent of reduction using N_2H_4 may be a function of pH and/or temperature.[3, 4] A recommended study would be altering synthesis conditions to achieve chemical reduction of $Pt(NH_3)_4^{2+}$ to metallic Pt using N_2H_4. Given that the addition of more components could affect micelle size, dynamic light scattering of the solutions before reduction of metal precursors is also recommended. In order to attain micelle droplets of uniform diameters, the same micelle sizes should be present in both metal and reductant microemulsion solutions.

5.2 Particle Size Control

Another benefit of reverse micelle synthesis is the control of particle size by controlling microemulsion droplet size. An initial study of particle size as a function of ω = 1.0, 1.1, 1.2 and 1.3 using the micelle procedure from Chapter 4 was performed for monometallic Pt nanoparticles from H_2PtCl_6-$6H_2O$ precursor and $Ni(NO_3)_2$-$6H_2O$ precursor. These values of ω were chosen based on previous work performed with Ru particles synthesized from $RuCl_3$ precursor. Elizabeth D'Addio of

the Lauterbach group found that increasing ω values increased micelle diameter found through dynamic light scattering, as shown in **Figure 5.1.**

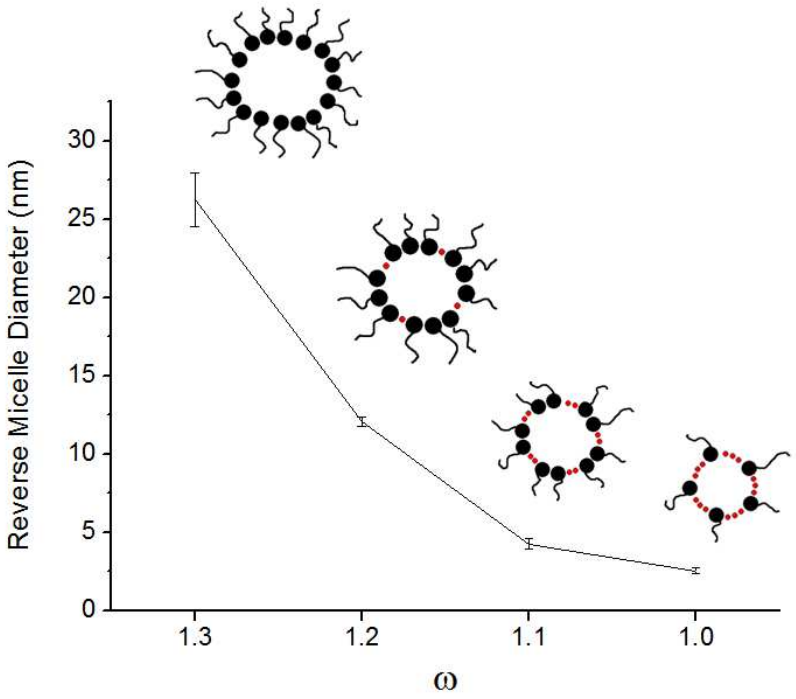

Figure 5.1 Dynamic light scattering used to determine reverse micelle size in solution of cyclohexane, DI water, Triton X-100 and 2-propanol. Experiment performed by E. D'Addio.

Analysis of TEM images also revealed increasing particle size from ω = 1.0 to 1.3. Further analysis of controlling micelle diameter and its effect on final particle size for different metals is necessary in order to draw conclusions. Control over particle size provides the opportunity to study structure-sensitive reactions.

5.3 Effect of Pre-Treatment Conditions

Almost every reverse micelle synthesis technique published has a different pre-treatment condition that is used to remove residual carbon from synthesis that can inhibit active sites. Some literature discusses the effect of these pre-treatments on the crystalline surface structure[5] and oxidation state and activity;[6] however, it is almost impossible to predict how different pre-treatment temperatures and atmosphere will affect final particle size and structure.

Other concerns regarding pre-treatment are the formation of $NiO/\gamma\text{-}Al_2O_3$ and $NiAl_2O_4$ compounds. For supported catalysts, the reduction of Ni is difficult and depends on the extent of interaction between Ni and the support.[7] Pre-treating in O_2 provides increased likelihood for oxidizing Ni nanoparticles and affecting the structure supported on $\gamma\text{-}Al_2O_3$. X-ray diffraction studies and temperature-programmed reduction are necessary to determine what species are present on catalysts throughout synthesis steps after supporting and before pre-treating.

The temperature and atmosphere for pre-treatment are other variables worth investigating. A pre-treatment temperature of 673 K was chosen based on results reported by Mitsuda, et al. that in an O_2-containing gas, Triton X-100 was oxidized thermally above 503 K leaving a slowly decomposing material. Using IR spectroscopy, they found a strong absorption band identified as a C=O stretching band when heating Triton X-100 adsorbed on carbon support in O_2. They suggested that the C-O-C bond in Triton X-100 was oxidized to -COOH, which has a CO double bond.[8] The effect of air and N_2 environments on decomposition of Triton X-100 has also been investigated.[9] If residual carbon from decomposing surfactant remains on the surface it will poison the active sites on the nanoparticles. It is of interest to optimize the pre-

treatment temperature and environment to remove solvents used in synthesis while not affecting reduced metal nanoparticles.

High-throughput screening has been utilized in the Lauterbach group to optimize pre-treatment time and temperature in O_2 for preparation of catalysts for NO_x storage reduction.[10] Such a technique would be beneficial for testing the effect of pre-treatment time, temperature and environment on particle size and sintering in catalysts. Choosing a structure-sensitive reaction, such as ammonia decomposition, would also be beneficial in testing the aforementioned variables that could affect final supported particle size. These catalysts could then be compared with catalysts synthesized by traditional industrial catalyst synthesis, such as incipient wetness impregnation and/or wet impregnation.

The synthesis of supported catalysts with controllable, reproducible, uniform particle size and narrow distribution would provide a powerful means to investigate the effect of particle size and shape on chemical reactivity. This synthesis would provide an effective way to bridge the materials gap between surface science experiments performed on model systems and complex, supported catalysts and guide industrial catalyst synthesis to produce catalysts with maximum activity and selectivity.

5.4 References

[1] J.R. Regalbuto, in: J.R. Regalbuto, (Ed.), Catalyst Preparation: Science and Engineering, CRC Press, Boca Raton. 297.

[2] W.A. Spieker, J.R. Regalbuto, *Chemical Engineering Science* **56** (2001) 3491.

[3] M. García-Diéguez, I.S. Pieta, M.C. Hererra, M.A. Larrubia, L.J. Alemany, *Applied Catalysis A: General* **377** (2010) 191.

[4] D.-H. Chen, S.-H. Wu, *Chemistry of Materials* **12** (2000) 1354.

[5] J. Solla-Gullón, V. Montiel, A. Aldaz, J. Clavilier, *Journal of Electroanalytical Chemistry* **491** (2000) 69.

[6] J.R. Croy, S. Mostafa, H. Heinrich, B.R. Cuenya, *Catalysis Letters* **131** (2009) 21.

[7] C. Li, Y.-W. Chen, *Thermochimica Acta* **256** (1995) 457.

[8] K. Mitsuda, H. Kimura, T. Murahashi, *Journal of Materials Science* **24** (1989) 413.

[9] R. Holze, A.T. Riga, E.B. Yeager, *Journal of Materials Science Letters* **5** (1986) 819.

[10] R. Vijay, *Doctoral Dissertation* (2007) 232.